

Article

# Geological, Geochemical, and Mineralogical Constraints on the Genesis of the Polymetallic Pb-Zn-Rich Nuocang Skarn Deposit, Western Gangdese, Tibet

Junsheng Jiang <sup>1</sup>, Shunbao Gao <sup>2,\*</sup>, Youye Zheng <sup>2,3</sup> , David R. Lentz <sup>4</sup> , Jian Huang <sup>5</sup>, Jun Liu <sup>2</sup>, Kan Tian <sup>2</sup> and Xiaojia Jiang <sup>2</sup>

<sup>1</sup> Wuhan Centre, China Geological Survey, Wuhan 430205, China; jsjiang0818@163.com

<sup>2</sup> Institute of Geological Survey, China University of Geosciences, Wuhan 430074, China; zhyouye@163.com (Y.Z.); junliucug@foxmail.com (J.L.); tillan@cug.edu.cn (K.T.); jiangxiaojia@cug.edu.cn (X.J.)

<sup>3</sup> State Key Laboratory of Geological Processes and Mineral Resources, School of Earth Science and Resources, China University of Geosciences, Beijing 100083, China

<sup>4</sup> Department of Earth Sciences, University of New Brunswick, Fredericton, NB E3B 5A3, Canada; davidrlentz@gmail.com

<sup>5</sup> East China Metallurgical Institute of Geology and Exploration, Hefei 230088, China; hj1020@yeah.net

\* Correspondence: gaoshunbao1980@cug.edu.cn

Received: 20 August 2020; Accepted: 20 September 2020; Published: 23 September 2020



**Abstract:** The Nuocang Pb-Zn deposit is a newly discovered polymetallic skarn deposit in the southern Lhasa subterrane, western Gangdese, Tibet. The skarn occurs at the contact between the limestone of Angjie Formation and the Linzizong volcanic rocks of Dianzhong Formation (LDF), and the subvolcanic granite porphyry intruding those formations; the contact metasomatic skarn is well zoned mineralogically and texturally, as well as geochemically. The skarn minerals predominantly consist of an anhydrous to hydrous calc-silicate sequence pyroxene–garnet–epidote. The endoskarn mainly consists of an assemblage of pyroxene, garnet, ilvaite, epidote, and quartz, whereas the exoskarn is characterized proximal to distally, by decreasing garnet, and increasing pyroxene, ilvaite, epidote, chlorite, muscovite, quartz, calcite, galena, and sphalerite. Geochemical analyses suggest that the limestone provided the Ca for all the skarn minerals and the magmatic volatiles were the main source for Si (except the skarnified hornfels/sandstone, and muscovite-epidote-garnet-pyroxene skarn possibly from the host sandstones), with Fe and Mn and other mineralizing components. During the hydrothermal alteration, the garnet-pyroxene skarn and pyroxene-rich skarn gained Si, Fe, Mn, Pb, Zn, and Sn, but lost Ca, Mg, K, P, Rb, Sr, and Ba. However, the skarnified hornfels/sandstone, and muscovite-epidote-garnet-pyroxene skarn gained Fe, Ca, Mn, Sr, Zr, Hf, Th, and Cu, but lost Si, Mg, K, Na, P, Rb, Ba, and Li. The REEs in the skarn were sourced from magmatic fluids during the prograde stage. Skarn mineral assemblages and geochemistry indicate the skarn in the Nuocang deposit were formed in a disequilibrated geochemical system by infiltrative metasomatism of magmatic fluids. During the prograde stage, garnet I ( $\text{And}_{97.6}\text{Gro}_{1.6}$ ) firstly formed, and then a part of them incrementally turned into garnet II ( $\text{And}_{64.4}\text{Gro}_{33.8}$ ) and III ( $\text{And}_{70.22}\text{Gro}_{29.1}$ ). The subsequent substitution of Fe for Al in the garnet II and III indicates the oxygen fugacity of the fluid became more reduced, then resulted in formation of significant pyroxene. However, the anisotropic garnet IV ( $\text{And}_{38.5}\text{Gro}_{59.8}$ ) usually replaced the pyroxene. In the retrograde stage, the temperature decreased and oxygen fugacity increased, but hydrolysis increased with epidote, ilvaite, chlorite I, and muscovite forming with magnetite. The continuing decreasing temperature and mixing with meteoric water lead to Cu, Pb, and Zn saturation as sulfides. After the sulfides deposition, the continued mixing with large amounts of cold meteoric water would decrease its temperature, and increase its pH value (neutralizing), promoting the deposition of significant amounts of calcite and chlorite II. The geological, mineralogical, and geochemical characteristics of Nuocang skarn, suggest that the Nuocang deposit

is of a Pb-Zn polymetallic type. Compared to the other typical skarn-epithermal deposits in the Linzizong volcanic area, it indicates that the Nuocang deposit may have the exploration potential for both skarn and epithermal styles of mineralization.

**Keywords:** skarn geochemistry; Nuocang Pb-Zn polymetallic deposit; Linzizong volcanic area; Tibet

---

## 1. Introduction

Skarn deposits, typically formed by the interaction of carbonate-bearing host rocks and magmatic hydrothermal fluids, occupy an important position among the sources of Fe, Cu, Pb, Zn, and Au. In comparison to the proximal Fe-Cu skarn, the Pb-Zn skarn are formed at relatively long distances from the causative magmatic rocks, thus forming in a lower temperature environment [1–4]. The infiltrative skarn deposits show affinity with magmatic hydrothermal activity, and their compositions positively correlate with that of the generating magmatic rocks [1,5]. They are characterized by the overall zonation that is based on the mineral assemblages in space, from the causative plutons through the proximal skarn zone towards the distal skarn zone, then the wall-rocks. Temporally, they are usually divided into the prograde and retrograde stages, reflecting the fluid evolution and their physical and chemical conditions. Generally, the whole-rock geochemistry of skarn and its mineralogical aspects yield a relatively unique fingerprint, which not only could provide a record of the element migration and enrichment in different zones, but also could reflect the environmental variation characteristics in the formation process [2]. In addition, the mineral assemblages and their elemental features in the skarn were influenced by different factors, such as the chemical compositions of the related magmatic rocks, the wall-rocks, or the surrounding environments [6], which could also be used in exploration targeting [7].

In this study, the Nuocang deposit is a newly discovered skarn Pb-Zn polymetallic deposit in the southern Lhasa subterrane, western Gangdese. So far, very limited research has been devoted to the geology, geochemistry, and mineralogy of this skarn system. The hydrothermal evolution and the conditions for the formation of skarn are still unclear. Therefore, we report the petrographic, and whole-rock geochemical characteristics of zoned skarns, as well as focus on the mineralogy of the dominant skarn minerals including pyroxene, garnet, epidote, ilvaite, chlorite, and muscovite both temporally and spatially. This helped to infer fluid evolution processes in the skarn stage, but it also provides a basis for defining controls on mineralization with implications for skarn exploration.

## 2. Regional Geology

The Tibetan Plateau, as an important structural-geological unit in China, mainly consists of the Tethyan Himalaya, Lhasa terrane, Qiangtang terrane, and Songpan–Ganzi complex from the south to north (Figure 1a; [8]). Generally, the Lhasa Terrane is composed of the southern Lhasa subterrane, central Lhasa subterrane, and the northern Lhasa subterrane (Figure 1b; [9]). The central Lhasa subterrane is comprised by the Proterozoic and Archean basement rocks, Permo-Carboniferous metasedimentary rocks, and Upper Jurassic-Lower Cretaceous sedimentary rocks, with a series of volcanic rocks and related granitoids, which were considered to be evolved from a microcontinent. The southern and northern Lhasa subterrane were traditionally thought to be as the accreting terranes, which were formed by the Neo–Tethyan Ocean lithosphere subduction beneath the central Lhasa subterrane during its evolution to subsequent collisions [9]. These accreting terranes were generally considered as the juvenile crust formed by the mantle-derived magmatism. However, the recent research by Hou et al. [10] suggests that the segment in southern Lhasa subterrane (83°–87° E) was also an ancient block that is similar to the central Lhasa subterrane through the Hf isotope systematics.

The Gangdese magmatic belt, located mainly in the southern Lhasa subterrane (Figure 1b), has experienced the northward subduction of the Neo–Tethyan oceanic lithosphere during the Late Triassic to Paleocene, the continental collision between India and Asia at 55–50 Ma, and subsequent

post collisional tectonics [11,12]. It is a 1600-km-long magmatic belt, which is dominated by the nested Gangdese batholiths and widespread Linzizong volcanic rocks. Four main magmatic events occurred in the Gangdese belt, i.e., ~205–152, ~109–80, ~65–41, and ~33–13 Ma, respectively, of which the 65–41 Ma magmatic activity occupied the most prominent position [13,14].

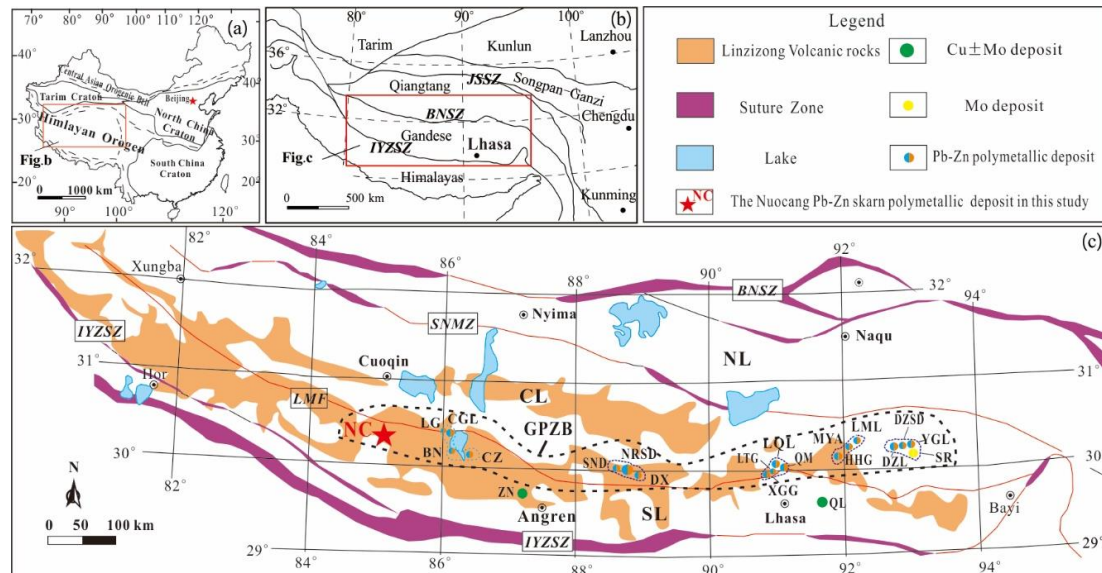


**Figure 1.** (a) Simplified tectonic map of China; (b) Simplified tectonic map of the Himalayan-Tibetan plateau; (c) Tectonic subdivisions of the Lhasa terrane (modified after [9]). SL: Southern Lhasa subterrane; CL: Central Lhasa subterrane; NL: Northern Lhasa subterrane; IYZSZ: Indus-Yarlung Zangbo Suture Zone; JSSZ: Jinshajiang suture zone; LMF: Luobadui-Milashan Fault; SNMZ: Shiquan River-Nam Tso Mélange Zone; BNSZ: Bangong-Nujiang Suture Zone. GPZB: Gangdese Pb-Zn polymetallic metallogenic belt. QL-Qulong; ZN-Zhunuuo; SR-Sharang; YGL-Yaguila; DZSD-Dongzhongsongduo; DZL-Dongzhongla; LML-Longmala; MYA-Mengyaa; HHG-Hahaigang; LQL-Leqingla; LTG-Lietinggang; XGG-Xingaguo; DX-Dexin; NRSD-Narusongduo; SND-Sinongduo; CZ-Chazi; BN-Beina; CGL-Chagele; LG-Longgen; NC-Nuocang.

Generally, the magmatism from Paleocene to Eocene (65~41 Ma) are featured by the extensive I-type calc-alkaline to high-K calc-alkaline Linzizong volcanic rocks and coeval plutons, which were caused by the roll-back of the Neo-Tethyan oceanic slab. The Gangdese belt within the Lhasa Terrane, usually divided into the Gangdese porphyry Cu (–Mo–Au) metallogenic belt (GPCB) in the south and the Gangdese Pb-Zn polymetallic metallogenic belt (GPZB) in the north, forms one of the most famous metallogenic belts in China (Figure 1b). The Gangdese porphyry Cu (–Mo–Au) metallogenic belt in the southern Lhasa subterrane consists of several giant porphyry Cu (–Mo–Au) deposits [15,16]. The Gangdese Pb-Zn polymetallic metallogenic belt (GPZB) is comprised by numerous Late Cretaceous to Eocene skarn, breccia-type, epithermal, hydrothermal Pb–Zn (–Ag), skarn Fe (–Cu), and porphyry–skarn Mo (–W) deposits, which are mainly distributed in the Central Lhasa subterrane and few in the northern part of southern Lhasa subterrane (such as the Chagele [17] and Nuocang in this study; Figure 1c).

### 3. Ore Deposits Geology

The Nuocang deposit, as a newly discovered skarn Pb-Zn polymetallic deposit in the Linzizong volcanic area, is located in the western Gangdese, Tibet, China. The strata exposed in the Nuocang deposit are the early Permian Angjie Formation, the late Cretaceous-early Paleocene Dianzhong Formation of Linzizong Group, and the Miocene Bugasi Formation (Figure 2). The Angjie Formation located in the northwest of the deposit, mainly consists of siltstone, sandstone, and limestone. The siltstone and sandstone are generally modified by either regional metamorphism, or contact

metamorphism ('cordierite-hornfels', [18]). The Dianzhong Formation of Linzizong Group (LDF), exposed to the southeast of the deposit, consists of significant rhyolite (Figure 3a), and minor rhyolitic breccia, rhyolitic ignimbrite, basaltic andesitic tuff, and andesitic tuff. The Bugasi Formation is developed isolated in the east with a very small area that is mainly composed of basalt, basaltic breccia and basaltic agglomerate. There are two groups of faults within the mine area: (i) ENE-trending, sub-vertical (70–74° dip) normal faults and subparallel faults which control the attitude of the layers, that are considered to be responsible for the path of ore-forming fluid; (ii) a nearly NS-striking sinistral strike-slip thrust fault dips toward the east at 70–74°, and cuts through the ENE-trending fault considered to post-date the mineralization. In addition, a 100–150 m, nearly EW-trending fracture alteration zone outcrops in the eastern part of the deposit, containing pronounced silica and skarn alteration, and some mineralization. The granite porphyry dikes outcrop in the eastern and southern part of Nuocang deposit, which usually emplaced into LDF or intruded the underlying Angjie Formation. The contacting zones between granite porphyry dikes and Angjie Formation develop extensive hornfels and skarn, which are recognized to be related with the Nuocang Pb-Zn mineralization (Figures 3b and 4a). Additionally, a plutonic body of granite porphyry has been discovered to the southeast of granite porphyry dikes (outside of the Figure 2), which is thought to be a possible link between the dikes and a deeper distal granitic intrusion. There is an overlap in zircon U–Pb ages obtained from the two granite porphyries (zircon U–Pb ages of  $72.4 \pm 0.6$  Ma and  $73.3 \pm 0.7$  Ma, [19]) and the rhyolite of Dianzhong Formation in the Nuocang deposit (zircon U–Pb age of  $72.4 \pm 0.4$  Ma, unpublished data from the Institute of Regional Geology and Mineral Resources, Shanxi, China), implying that they are genetically related to the same magmatic event.

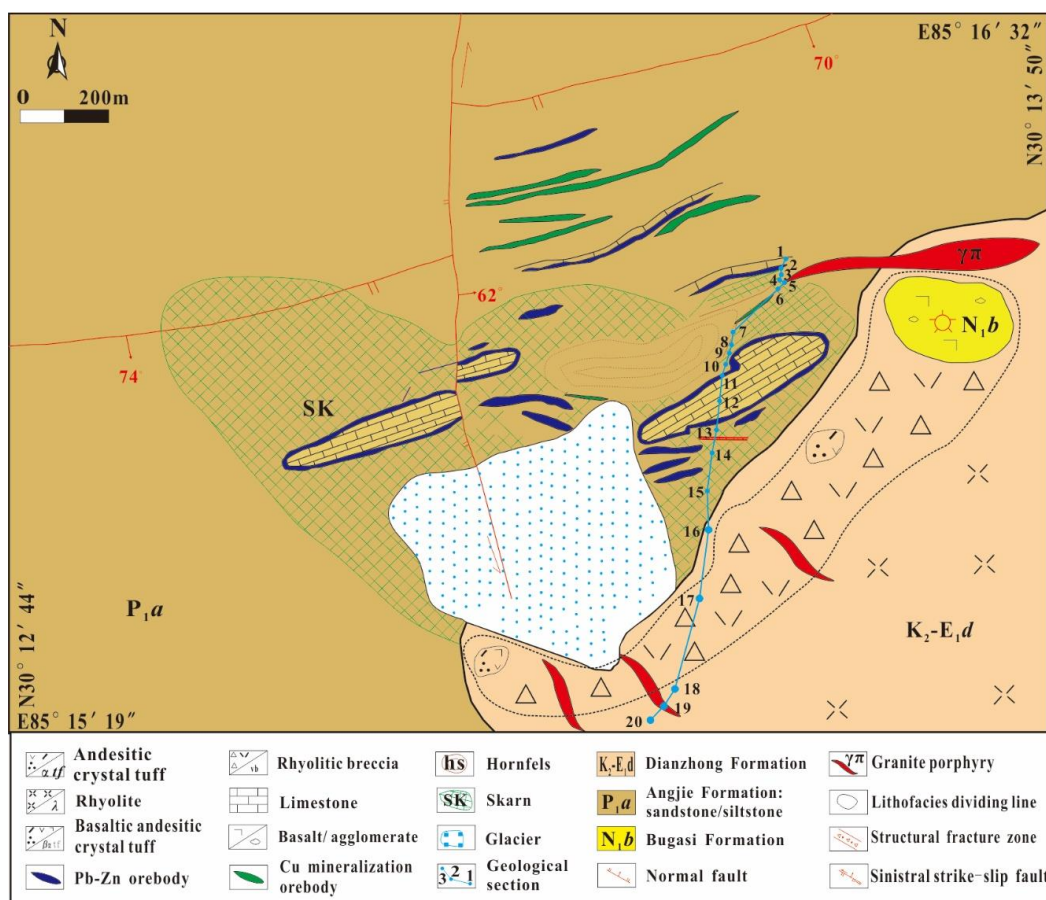


**Figure 2.** Geological map of the Nuocang skarn Pb-Zn polymetallic deposit, western Gangdese, Tibet (modified after [18]).

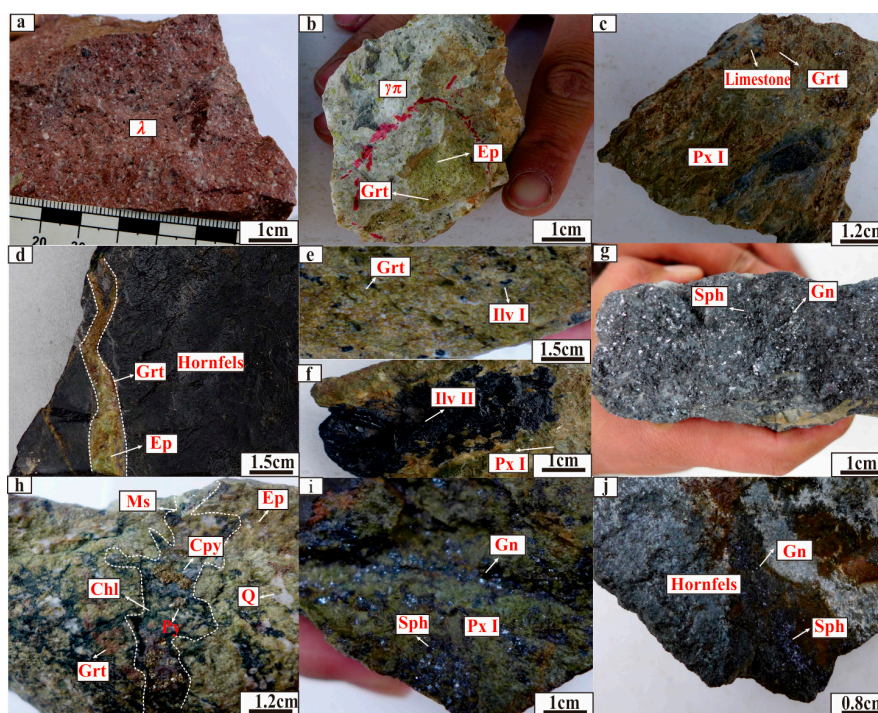


**Figure 3.** Photographs of the Nuocang granite porphyry, rhyolite, skarns and representative mineralized samples. (a) Rhyolite; (b) Altered granite porphyry that contains garnet and epidote; (c) Limestone replaced by the garnet-pyroxene skarn leaving a residual limestone in the skarn; (d) Garnet-epidote vein cutting through the hornfels; (e) Grained ilvaite I interstitial in the garnet-rich skarn; (f) Long columnar ilvaite II displaying a later alteration in the garnet-pyroxene skarn; (g) massive galena-sphalerite ore coexisting with quartz; (h) Chlorite-muscovite-quartz-chalcopyrite-pyrite quartz vein crosscuts the garnet-epidote-quartz assemblage; (i) Disseminated sphalerite and galena in the skarn; (j) Sphalerite-galena vein cutting through the hornfels.  $\lambda$ : rhyolite;  $\gamma\pi$ : granite porphyry; Grt: garnet; Px: pyroxene; Q: quartz; Ilv: ilvaite; Ms: muscovite; Ep: epidote; Chl: chlorite; Py: pyrite; Cpy: chalcopyrite; Gn: galena; Sph: sphalerite.

The skarn is situated along the contact between the Dianzhong and Angjie formations. Except for the skarn alteration, there exist a series of episodes of silicification, carbonatization, and clay alteration. Generally, the ore-related skarn alteration types are overprinted by the distinct silicification, and locally by later carbonatization. The Pb-Zn orebodies are the main mineralization in the Nuocang deposit, with lengths of 10–640 m and widths of 0.8–3.3 m. They dip toward the southwest with their dip angle varying from 57–82°. The ore minerals primarily consist of galena, sphalerite, with minor chalcopyrite, pyrite, and magnetite (Figure 3g–j), and the gangue minerals are mainly pyroxene, quartz, epidote, garnet, and calcite (Figure 3c–i). Subordinate Cu mineralization is mainly hosted in interlaminar fractures in the sandstone and slate, with the supergene ore minerals malachite and azurite, and rare chalcopyrite and bornite, and quartz, plagioclase, and clay minerals as gangue minerals.

Based on field geology observations, hand specimens, and petrography, the polymetallic Nuocang Pb-Zn skarn mineralization is composed of four paragenetic stages. The prograde minerals in stage I are pyroxene, garnet, and wollastonite (Figure 4b–g,k; Figure 5). Epidote, ilvaite, actinolite, hematite and magnetite that formed after the replacement of the early garnet and pyroxene were the main hydrous silicate minerals during the early retrograde stage (stage II) (Figure 4e–h,j). Hematite and magnetite contents in this deposit were much less than those of ilvaite (Figure 3e,f and Figure 4j). In the later retrograde stage, muscovite, chlorite, and quartz, together with pyrite, pyrrhotite, and chalcopyrite formed irregular veins that cut through the epidote, pyroxene, and garnet (Figures 3h and 4i,l,m). In the quartz-sulfide stage (stage III), significant galena and sphalerite typically developed with quartz in the

western of ore district, with a massive texture, whereas galena and sphalerite occur as a disseminated texture in pyroxene skarn at the east of ore district (Figure 3h,i and Figure 4n).

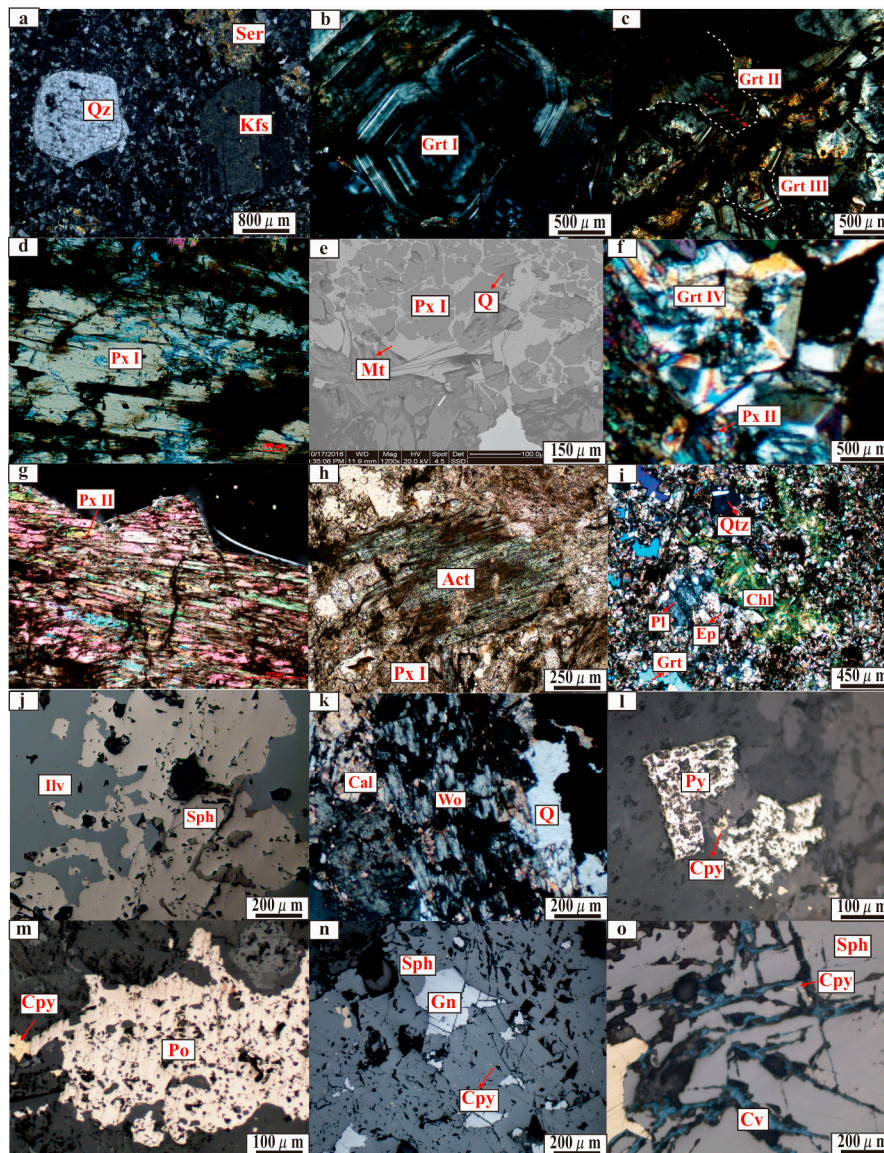


**Figure 4.** Photomicrographs of mineral assemblages for the Nuocang skarn and ore minerals. (a) Euhedral K-feldspar and quartz crystals, some K-feldspar altered into sericite; (b) Euhedral isotropic garnet I; (c) Garnet II (core is isotropic and rim is anisotropic) coexisting with type III garnet (core is anisotropic and rim is isotropic) altered by later hydrothermal fluid; (d) Prismatic pyroxene I; (e) Replacement of pyroxene by magnetite; (f) Allotriomorphic pyroxene II replaced by type IV garnet; (g) Radial pyroxene II; (h) Replacement of columnar pyroxene I by radial actinolite; (i) Plagioclase and quartz filling between the chlorite and epidote, and the garnet replaced by the epidote; (j) Ilvaite showing embayed texture after replacement by later sphalerite; (k) Long columnar wollastonite in the skarn, with minor quartz and calcite; (l) Euhedral and subhedral pyrite, and small grained chalcocopyrite; (m) Grained chalcocopyrite coexisting with anhedral pyrrhotite; (n) Replacement of galena by sphalerite, with exsolved chalcocopyrite in the sphalerite; (o) Veined chalcocopyrite and covellite filling the sphalerite.

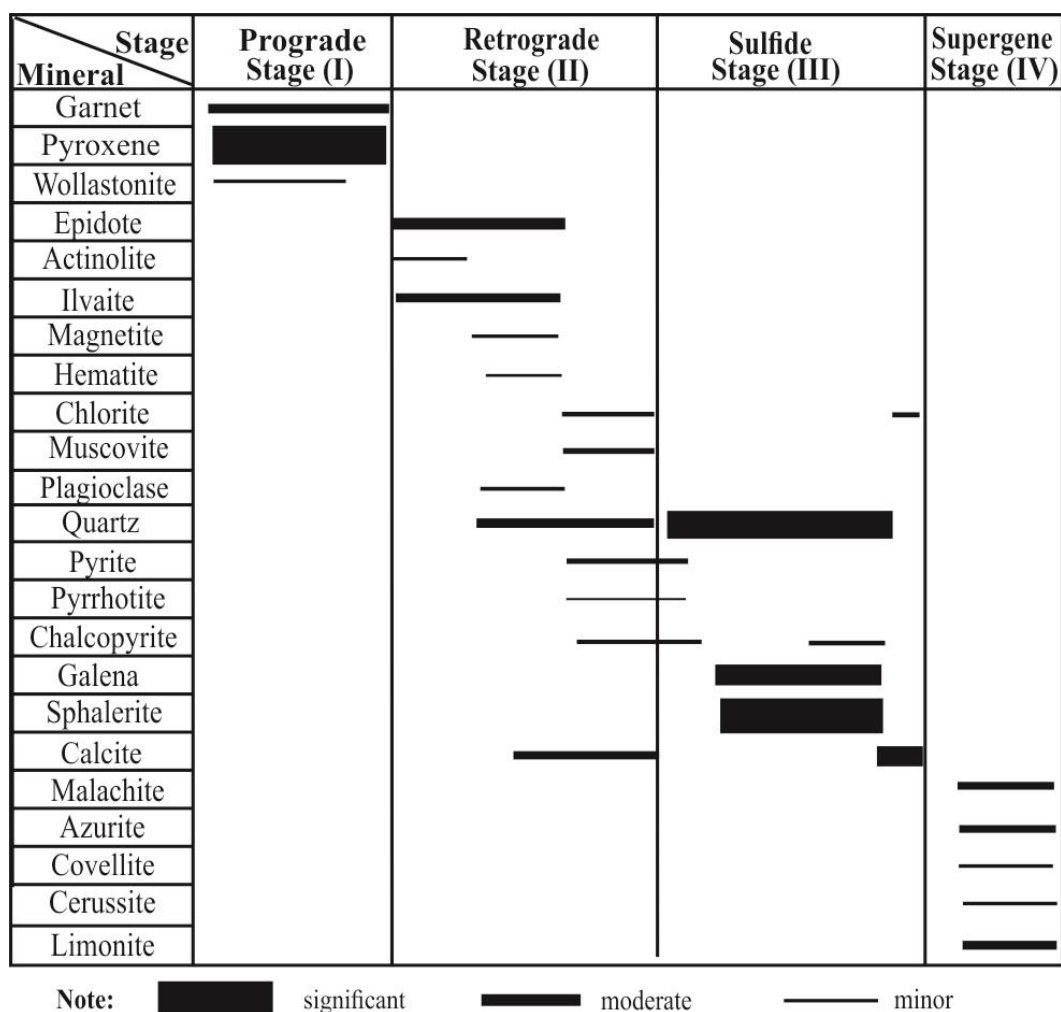


Figure 5. Mineral paragenesis for Nuocang Pb–Zn skarn polymetallic deposit.

Some chalcopyrite occurred as the emulsion texture in the sphalerite (chalcopyrite disease), with some secondary covellite filling fractures in sphalerite (Figure 4o). Later calcite, sometimes together with chlorite, was interstitial in the galena-sphalerite-quartz vein. Locally, preserved supergene weathering also occurred in stage IV, which is characterized by malachite, azurite, cerussite, covellite, and limonite.

#### 4. Zonation Characteristics

An approximately N–S horizontal section across from the limestone zone to the volcanic rocks zone in the eastern part of Nuocang ore district (Figure 2; Table 1) was distinguished based on detailed mapping of the ore-field.

**Table 1.** Mineral composition in different skarn zone of Nuocang deposit.

Zone No.	Zone Name	Mineral Composition
Zone 1	Limestone zone	Calcite (99%), quartz (minor)
Zone 2	Pyroxene-rich skarn zone	Pyroxene (75%), epidote (6%), garnet (6%), quartz (5%), ilvaite (3%), calcite (2%), sphalerite (2%), galena (1%), chlorite (trace)
Zone 3	Garnet pyroxene skarn zone	Garnet (30%), pyroxene (50%), epidote (10%), quartz (5%), calcite (4%), ilvaite (minor)
Zone 4	Hornfels zone	Quartz (50%), Plagioclase (45%), epidote (2%), chlorite (2%), biotite (1%)
Zone 5	Granite porphyry zone	Phenocryst (20%): quartz (8%), K-feldspar (5%), plagioclase (5%), sericite, chlorite(minor); Groundmass (80%): K-feldspar (30%), quartz (20%), plagioclase (20%)
Zone 6	Hornfels zone	Quartz (50%), Plagioclase (45%), epidote (2%), chlorite (2%), biotite (1%)
Zone 7	Metasandstone-metamorphic siltstone zone	Quartz (40–55%), plagioclase (30–35%), clay minerals (0–25%), biotite, epidote, chlorite, chalcopyrite, pyrite (minor); sphalerite, galena (trace)
Zone 8	Skarnified sandstone zone	Quartz (25%), plagioclase (10%), pyroxene (40%), garnet (10%), epidote (5%); calcite, hornblend, biotite/sericite, chlorite (minor)
Zone 9	Pyroxene-rich skarn zone	Pyroxene (70%), garnet (4%), epidote (4%), quartz (8%), galena (3%), sphalerite (8%), chlorite (minor)
Zone 10	Limestone zone	Calcite (99%); quartz and plagioclase (minor); pyroxene, epidote, chlorite (minor)
Zone 11	Pyroxene-rich skarn zone	Pyroxene (75%), garnet (5%), epidote (5%), quartz (4%), calcite (2%), galena (2%), sphalerite (7%)
Zone 12	Limestone zone	Calcite (99%); quartz (minor); pyroxene, epidote, and chlorite (trace)
Zone 13	Pyroxene-rich skarn zone	Pyroxene (75%), garnet (5%), epidote (5%), quartz (4%), calcite (1%), galena (2%), sphalerite (8%)
Zone 14	Muscovite garnet pyroxene skarn zone	Pyroxene (50%), epidote (20%), garnet (10%), chlorite (5%), muscovite (5%), quartz (5%), calcite (3%), pyrite (1%), chalcopyrite (1%)
Zone 15	Skarnified sandstone zone	Quartz (40%), plagioclase (30%), epidote (15%), chlorite (5%), garnet (3%), calcite (3%), pyrite (2%), sericite (2%)
Zone 16	Skarnified rhyolite tuff zone	Quartz (30%), plagioclase (25%), epidote (5%), chlorite (5%), sericite (2%), carbonate (2%), kaolinite (1%), ash (30%)
Zone 17	Rhyolitic breccia zone	Volcanic breccia (60%), ash (30%); quartz and plagioclase crystal pyroclast (8%); sericite, chlorite and carbonate (minor)
Zone 18	Rhyolite	Phenocryst (20%), quartz (10%), K-feldspar (7%), plagioclase (3%), sericite and chlorite(minor); groundmass (80%): cryptocrystalline
Zone 19	Granite porphyry	Phenocryst (20%): quartz (10%), K-feldspar (5%), plagioclase (4%), sericite and chlorite (minor); groundmass (80%): K-feldspar (30%), quartz (20%), plagioclase (20%)
Zone 20	Rhyolite	Phenocryst (25%): quartz (12%), K-feldspar (10%), plagioclase (3%), sericite and chlorite (minor); groundmass (75%): cryptocrystalline

#### 4.1. Ore-Related Intrusion

The ore-related intrusion is granite porphyry, occurring as dykes in the eastern ore district and intruding into the wall-rocks. The granite porphyry near the skarn zone is usually skarnified, mainly represented by local plagioclase altered to garnet and (or) epidote (Figure 3b). It is grayish white (fresh) or reddish brown when altered, with the distinct porphyritic texture and massive structure. The phenocrysts (20 vol.%) consist of quartz (10 vol.%, 1–1.5 mm), plagioclase (5 vol.%, 1–2 mm, some altered to sericite and kaolinite), and K-feldspar (5 vol.%, 1–2 mm, some altered to sericite and kaolinite). The groundmass (80 vol.%) mainly includes 30–35 vol.% K-feldspar (0.05–0.2 mm), 25–30 vol.% quartz (0.05–0.25 mm), and 15–20 vol.% (0.1–0.2 mm) plagioclase (Figure 4a). Accessory minerals are characterized by titanite, zircon, and apatite. In addition, rare pyrite occurs as euhedral crystals in the granite porphyry that possibly formed during the alteration of phenocrysts and groundmass.

#### 4.2. Skarn

Endoskarn (zone 8, 14, 15, and 16) could be observed in the external aureole of the thermal metamorphosed rocks and relatively close to the granite porphyry, which preserve a few of plagioclase and other contents of the protolith (sandstone and rhyolite tuff). The endoskarn consists of an assemblage of garnet + pyroxene + ilvaite + quartz ± epidote + muscovite. Compared to the exoskarn zone, its thickness is narrow (0.5–1 m). The content of garnet in the endoskarn is relatively high, but not up to those found in other skarn Fe-Cu or Cu-Au deposits. In general, garnet in the Nuocang deposit usually exhibits euhedral-subhedral crystals, a primary dark brown, brown, and minor yellow colour, and a size of 100 µm to 5 mm. Generally, garnet occurs as massive, banded, or lensoid in the endoskarn. The garnet is locally partly replaced by epidote, which represents a transition from the prograde to retrograde (hydrous) stage. Pyroxene in the endoskarn occurs mostly as green or dark green, prismatic crystals, up to 5 mm long, included within poikiloblastic garnet or replacing the garnet. Pyroxene is predominant in the skarn mineral assemblages, and generally forms massive aggregates of randomly oriented crystals, in association with interstitial sphalerite, quartz, calcite and garnet. Epidote in the endoskarn, as the metasomatic retrograde skarn species, is green, subhedral-euhedral, prismatic or granular, of 50–150 µm in size. Ilvaite, showing black, long prismatic crystals, is a retrograde mineral in the endoskarn and always in association with quartz interstitial to the garnets. Muscovite coexists with the chlorite, chalcopyrite, pyrite, and quartz in muscovite-pyroxene-garnet skarn. Only a small amount of ore minerals, such as chalcopyrite, pyrite, galena, and sphalerite, could be identified in the endoskarn and occur as disseminated interstitial to the garnet and pyroxene.

The exoskarn zones consist of pyroxene-rich skarn (zones 2, 9, 11, and 13), and garnet-pyroxene skarn (zone 3). The exoskarn is marked by a decreasing content of garnet, increasing contents of pyroxene, epidote, and other skarn minerals, more intense hydrothermal alterations, such as vein quartz and calcite, higher grades of galena, sphalerite, and other ore minerals. Pyroxene, as the most widespread skarn mineral in the exoskarn, shows variable colors of dark green, green, and brown. Pyroxene occurs as prismatic and needle-like crystals (size of 1–3 cm) widely observed in the exoskarn, which is mainly composed of massive aggregates of randomly oriented crystals, in association with interstitial sphalerite, quartz, calcite and garnet. However, minor anhedral grained pyroxene crystals (size of 1–5 mm), experienced a strong retrograde alteration. Reddish weathering patinas of iron oxyhydroxides occur along cleavage and cracks in pyroxene crystals. Compared to the endoskarn, the content of the garnet in the exoskarn is sharply decreased, being present as a minor phase. Garnet is characterized by a relatively light shade of yellow, yellow green, or minor brown, euhedral-subhedral, and variable grained size (10 µm–10 mm) crystals. The garnet is commonly interstitial in the pyroxene crystals, with a small number of garnets occurring as lentoid and vein in the exoskarn. The epidote is a retrograde mineral in the exoskarn, occurring as the yellow green, columnar or granular crystals, with the size of 5–50 µm. It replaced garnet in the exoskarn but was in turn replaced by chlorite or ore-bearing quartz. The galena and sphalerite in the exoskarn are generally interstitial in the fissures of the pyroxene crystals, or together with ore bearing vein quartz.

### 4.3. Limestone and Thermal Metamorphic Rocks

The limestone occurs as a lensoid in the center of the ore district, with an E-W trending and high dip angle. The limestone is usually massive, but grades into marble which is in part silicified proximal to the sulfide mineralized zone. In addition, the limestone has a gradational contact relation with the skarn, which is mainly manifested as a skarnification along the boundary, including the pyroxene-epidote-garnet skarn in the limestone.

The thermal metamorphic rock closest to the granite porphyry is hornfels (zone 4, 6; Figure 2). It is a grey black, dense massive, hard rock, and manifested by intense replacement of the calcareous siltstone. Outwards, the thermal metamorphism becomes relatively weak, associated with large amounts of metasandstone (zone 7), which reflects the gradual decreasing of thermal metamorphism from the intrusion outward. Generally, thermal metamorphic rocks in this zone are characterized by large numbers of quartz, feldspar, mica, and clay minerals and later altered minerals, such as biotite, chlorite, epidote, carbonate, and kaolinite. In addition, pyrite, chalcopyrite, galena, and sphalerite associated with quartz occur as stockwork or veinlets in the fractures of contact metamorphic rocks, representing a later hydrothermal mineralization.

## 5. Samples and Methods

### 5.1. Whole-Rock Major and Trace Element Compositions

Ten representative samples from different zones of the geological section were selected for major and selected trace elements analysis. A minimum 1 kg for each rock was taken from the Nuocang deposit, in order to obtain a chemically homogeneous result. Each sample was crushed into small pieces for pulping. All samples were crushed into small pieces and then powdered in agate mortar. Whole rock analyses were done at Wuhan Sample Solution Analytical Technology Co. Ltd. (Wuhan, China), while major elements were measured by XRF, with an analytical uncertainty of < 5% and trace elements were analyzed using ICP-MS (7500a, Agilent, Palo Alto, CA, USA) and the analytical precision is better than 5% for elements. Details of the analytical processes can be found in Liu et al. [20].

### 5.2. Electron Probe Microanalyses

Twenty three representative samples of the different skarn zones were collected from the Nuocang deposit in order to cover all aspects of skarn formation, of which seventeen samples were taken from an approximately N-S horizontal section perpendicular to the strike in the eastern part of the deposit, and six samples were taken from the central and western part of the deposit. Representative samples were prepared as polished thin sections and studied by optical microscopy in order to define the occurrence, morphology, and texture of skarn minerals (garnet, pyroxene, epidote, ilvaite, and chlorite). The thin sections were later examined by scanning electron microscopy (SEM), using the FEI Quanta 200 environmental scanning electron microscope at the State Key Laboratory of Geological Process and Mineral Resources of the China University of Geosciences, (Wuhan, China). Individual spots were selected in the skarn minerals for subsequent electron probe microanalysis (EPMA), conducted at the Center for Material Research and Analysis, Wuhan University of Technology (WUT) using a JXA-8230 Superprobe (JEOL, Tokyo, Japan). Standards and unknowns were analyzed by 1  $\mu\text{m}$  beam diameter, with an accelerating voltage of 20 kV and a beam current of 20 nA. Integration time for peaks of Al, Si and Mg are 30 s, and the remaining elements are 20 s.

## 6. Results

### 6.1. Lithochemistry

Major and trace elements analysis of the limestone, skarn, skarnified hornfels and sandstone in the Nuocang deposit are shown in Table 2, with the mass balance computed data of various components shown in Table 3. Mass-balance calculation has been widely used as a way to discuss some fluid-rock

interaction processes, since it could reveal the mass gain or loss during the opening of a geological system [4,21]. So far, several of mass-balance calculation methods, including composition-volume diagram [22], Isocon diagram [23,24], normalized Isocon diagram [21], quantitative calculation method, and Isocon Analysis Method of Grant [23], has been applied to describe geological processes. In this study we have selected the Isocon Analysis Method of Grant due to its simplicity and efficiency, and the basic equation shows as follows:

$$C_i^A = \left( \frac{M^O}{M^A} \right) (C_i^O + \Delta C_i^{O-A}) \quad (1)$$

In Equation (1),  $C_i^A$  and  $C_i^O$  mean the concentration of component  $i$  in the altered sample and the unaltered sample, respectively,  $M^A$  and  $M^O$  mean the gross mass of the altered sample and the unaltered sample, respectively, and  $\Delta C_i^{O-A}$  means the concentration variation of component  $i$  from the unaltered sample O to the altered sample A.

During the process of hydrothermal alteration, the majority of the major elements in the altered rocks display visible mass gains or losses ( $\Delta C_i^{O-A}$ ). Compared with the unaltered protolithic limestone, the chemical composition of garnet-pyroxene skarn and pyroxene-rich skarn are enriched in  $\text{SiO}_2$ ,  $\text{Fe}_2\text{O}_3^T$ , and  $\text{MnO}$ , and depleted in  $\text{CaO}$ ,  $\text{MgO}$ ,  $\text{K}_2\text{O}$  and  $\text{P}_2\text{O}_5$ . However, compared with the unaltered sandstone, the skarnified hornfels and sandstone, and muscovite-garnet-pyroxene skarn are enriched in  $\text{Fe}_2\text{O}_3^T$ ,  $\text{CaO}$ , and  $\text{MnO}$ , and depleted in  $\text{SiO}_2$ ,  $\text{MgO}$ ,  $\text{Na}_2\text{O}$ ,  $\text{K}_2\text{O}$  and  $\text{P}_2\text{O}_5$ . Most of the mobile elements, such as the Rb, Ba, and Li showed visible mass loss in the altered rocks. However, Sr generally shows mass loss in the garnet-pyroxene skarn and pyroxene-rich skarn far from the intrusion, but generated mass gain in the skarnified hornfels and sandstone, and muscovite-garnet-pyroxene skarn near the intrusion. The high field strength elements (HFSE) of Nb, Ta, and U behaved as immobile elements during skarn formation. However, the Zr, Hf, and Th display very minor mass change in the garnet-pyroxene skarn and pyroxene-rich skarn near the limestone, but generated notable mass gains in the skarnified hornfels and sandstone, and muscovite-garnet-pyroxene skarn near the intrusion (Table 3).

In the primitive mantle-normalized spider diagram (Figure 6a), the granite porphyries are generally enriched in Rb and K, but depleted in Ba, Sr (LILE), and Nb, Ta, P, Ti (HFSE), which are similar to the skarnified hornfels and sandstone, muscovite-garnet-pyroxene skarn, and sandstone in the endoskarn zone.

However, the garnet-pyroxene skarn, and pyroxene-rich skarn in the exoskarn zone are only enriched in Rb, but depleted in K, Ba, Sr, Nb, P, and Ti. The limestones yield a permanent negative anomaly for Nb, Ta, Zr, Hf, Ti, and Ba. REE patterns of all the samples are shown in Figure 6b. Enrichment of LREE over HREE is seen, with negative Eu anomalies. The granite porphyries have similar REE patterns with moderate  $\Sigma\text{REE}$  values (averaging 215 ppm), high  $(\text{La}/\text{Yb})_N$  values (average 12.38), and strong negative Eu anomalies (average 0.49). The sandstones have relatively moderate  $\Sigma\text{REE}$  values (average 155 ppm), with high  $(\text{La}/\text{Yb})_N$  values (average 11.1), and moderate Eu anomalies (average 0.72). The limestones display smooth REE curves, with very low fractionation values between LREE and HREE (average  $(\text{La}/\text{Yb})_N$  is 6.02).

The skarnified hornfels and sandstone, muscovite-garnet-pyroxene skarn, and sandstone located near the intrusion have relatively high  $\Sigma\text{REE}$  values (average 168.6 ppm), with a large range of  $(\text{La}/\text{Yb})_N$  values (3.87 to 14.71, average 9.77), and  $\text{Eu}/\text{Eu}^*$  values (0.47 to 1.16, average 0.86), lying between the intrusive rocks and the sandstones. However, the garnet-pyroxene skarn, and pyroxene-rich skarn located relatively far from the intrusions show low  $\Sigma\text{REE}$  values (average 168.6 ppm), with low  $(\text{La}/\text{Yb})_N$  values (average 16.67), and a wide range of  $\text{Eu}/\text{Eu}^*$  values (0.19 to 1.03, average 0.64). These skarn REE curves lie between the intrusive rocks and the carbonate rocks.

**Table 2.** Major and trace element analysis of the limestone, sandstone, skarn, and granite porphyry in the Nuocang deposit, western Gangdese.

Sample No.	NCN01 02-Is1	NCN01 02-Di1	NCN01 04-grt2	NCN-PM01- b09	NCN01 05-ss1	NCN01 05-hl3	NCN02 10-γπ1	NCN02 10-γπ1(1)	NCN02 10-γπ3	NCN02 12-γπ1	NCN02 12-γπ2	NCN01 13-Sph1	NCN- Zn1	NCN01 14-Is1	NCN01 17-Di1	NCN03 05-MS2	NCN01 20-SK1	NCN01 20-ss1	NCN02 19-γπ1
Sample Name	Is	Px SK	Grt-Px SK	Grt-Px SK	ss	SK hl	γπ	γπ	γπ	γπ	γπ	Sph SK	Sph SK	Is	Grt-Px SK	Ms -Grt-Px SK	SK ss	ss	γπ
Zone	1	2	3	3	4	4	5	5	5	5	5	9	11	12	13	14	15	16	19
SiO <sub>2</sub>	1.72	47.44	42.22	46.92	77.12	42.64	76.56	76.73	74.89	75.12	75.64	59.37	39.44	1.93	38.55	37.67	35.03	76.46	73.85
TiO <sub>2</sub>	0.02	0.03	0.03	0.05	0.21	0.75	0.12	0.11	0.13	0.11	0.11	0.03	0.32	0.03	0.10	0.08	0.94	0.33	0.14
Al <sub>2</sub> O <sub>3</sub>	0.28	0.72	1.55	0.95	8.97	19.51	10.68	11.00	12.23	10.52	10.56	1.46	2.46	0.57	3.61	23.49	17.61	10.5	13.02
Fe <sub>2</sub> O <sub>3</sub> <sup>T</sup>	0.23	25.75	23.41	22.18	3.81	8.51	1.31	1.27	1.58	0.96	0.75	17.53	17.32	0.60	23.35	10.17	10.52	4.12	2.04
MnO	0.05	2.36	1.81	2.40	0.05	0.25	0.02	0.02	0.03	0.06	0.06	2.52	1.99	0.06	0.80	0.31	0.60	0.08	0.02
MgO	0.54	0.89	1.37	0.78	0.19	0.27	0.33	0.34	0.43	0.38	0.38	0.41	1.43	0.49	0.68	0.11	1.43	0.21	0.25
CaO	53.84	21.90	24.60	23.40	0.44	16.37	1.92	1.48	1.98	3.45	3.13	17.47	18.86	53.79	28.94	20.07	23.44	0.58	0.83
Na <sub>2</sub> O	0.05	0.08	0.10	0.11	1.56	0.08	1.34	1.31	0.65	0.86	1.23	0.18	0.19	0.03	0.06	0.06	0.04	1.24	1.24
K <sub>2</sub> O	0.06	0.05	0.04	0.04	4.08	3.28	5.13	5.07	4.95	4.48	4.08	0.02	0.09	0.12	0.03	1.91	0.44	3.74	5.58
P <sub>2</sub> O <sub>5</sub>	0.02	0.02	0.02	0.03	0.05	0.28	0.02	0.02	0.02	0.02	0.01	0.02	0.08	0.04	0.09	0.01	0.39	0.06	0.02
LOI	42.85	0.03	4.64	2.92	2.01	7.53	2.27	2.23	2.67	3.90	3.59	0.06	11.59	41.64	3.04	5.22	8.98	1.76	2.56
Li	2.36	4.22	3.05	5.78	35	9.24	16.13	17.51	34.42	14.02	18.21	13.5	9.02	2.19	2.75	11.7	29.7	13	18.86
Be	0.11	1.11	1.01	1.78	1.37	0.95	1.70	1.84	2.40	2.06	2.06	2.24	1.36	0.16	0.42	0.43	0.75	1.65	1.73
Sc	0.67	0.86	0.89	2.58	16.4	10.1	4.24	4.29	6.90	3.82	3.02	0.98	6.56	1.12	6.93	3.85	10.4	17.8	5.02
V	4.20	6.11	11.6	14.14	52.3	92.3	4.47	3.94	8.09	21.63	20.22	8.19	93.69	6.95	53.4	4.41	80.6	70.5	4.96
Cr	1.25	2.15	2.19	10.86	0.03	3.75	4.91	5.16	6.13	7.33	5.64	2.92	20.51	2.22	12.4	0.51	1.80	0.05	4.68
Co	3.78	36.2	31.4	17.57	15.4	32.8	0.47	0.41	0.69	1.08	1.16	43.6	28.86	3.24	25.9	0.90	3.50	17.6	1.21
Ni	7.05	5.29	15.4	6.6	32.4	2.65	0.70	0.65	0.57	1.36	1.49	3.94	6.81	7.70	7.78	2.44	6.12	23.4	0.57
Cu	1.33	1.18	5.88	17.47	20.6	3.38	4.05	3.17	3.00	4.32	7.21	4.41	21.48	4.49	2.31	1.40	3.48	12.8	9.91
Zn	5.33	337	170	338	56.4	123	54.00	70.13	25.83	15.08	14.66	3372	34240	14.6	279	17.8	55.2	41	23.16
Ga	0.33	2.82	3.16	3.08	35.6	28.3	10.96	12.27	18.78	11.95	12.12	2.80	3.84	0.58	7.55	25.6	27.1	4.6	19.58
Rb	2.14	4.19	4.77	5.39	799	198	130.8	138.0	169.2	148.6	134.6	1.49	7.92	6.58	3.03	92.5	15.0	989	196.5
Sr	1005	26.3	28.2	43.54	102	459	261.4	242.2	197.0	159.6	159.3	10.7	172.7	721	43.6	641	728	72	77.39
Y	3.40	2.54	5.81	4.41	20.3	21.4	27.62	27.56	29.03	18.48	16.03	3.71	8.40	4.86	7.05	35.4	27.1	15.3	30.73
Zr	2.42	14.0	5.34	11.14	431	152	190.0	184.0	178.6	87.52	89.60	8.47	53.80	3.88	10.5	125	224	281	195.6
Nb	0.17	0.64	0.73	2.09	5.21	9.53	1.55	1.50	1.20	1.56	2.02	0.68	1.78	0.31	0.83	8.85	12.1	2.35	1.35
Sn	0.063	15.3	283	79	0.1	149	4.06	4.47	3.14	6.95	1.03	3.80	2.01	0.12	77.2	649	80.7	0.1	4.05
Cs	0.096	1.20	4.72	6.61	5.1	3.28	3.62	3.94	10.10	6.25	4.82	0.77	19.50	0.67	1.74	1.26	0.18	9.7	5.32
Ba	15.7	6.04	11.5	46.6	301	202	1447	1411	642.6	905.0	1041	2.09	73.60	7.07	6.59	148	49.1	207	782.9
La	2.20	1.89	1.47	3.45	38.33	29.2	43.47	47.62	52.21	45.80	31.85	0.89	9.32	2.67	3.39	19.5	47.7	6.67	58.14
Ce	2.56	3.63	2.08	3.09	46.84	58.8	95.59	99.83	106.2	83.85	60.46	1.51	17.04	2.85	6.37	45.0	100.6	113.36	116.6
Pr	0.41	0.42	0.36	0.53	3.28	6.87	11.05	11.47	11.85	8.47	6.28	0.26	2.34	0.52	0.86	5.88	12.0	7	13.26
Nd	1.65	1.61	1.49	2.07	10.89	28.1	42.12	42.76	44.20	28.98	21.35	1.12	9.39	2.09	3.68	23.7	47.3	45.79	49.36
Sm	0.37	0.32	0.31	0.38	3.9	5.49	7.60	7.68	7.92	4.41	3.49	0.35	1.99	0.46	0.94	6.10	8.13	4.06	8.88
Eu	0.083	0.061	0.12	0.06	0.87	1.59	0.93	0.98	1.05	0.94	0.59	0.025	0.54	0.12	0.25	0.92	2.73	1.01	1.17
Gd	0.34	0.31	0.42	0.39	2.98	4.65	6.60	6.67	6.87	3.90	3.14	0.44	1.98	0.50	1.05	5.74	6.41	5.06	7.78
Tb	0.057	0.052	0.079	0.069	0.56	0.69	1.00	1.01	1.09	0.64	0.51	0.065	0.30	0.080	0.15	0.99	0.91	0.56	1.22
Dy	0.33	0.28	0.55	0.44	2.04	3.98	5.25	5.47	5.68	3.33	2.73	0.39	1.47	0.52	0.88	6.13	5.16	3.98	6.17
Ho	0.071	0.055	0.15	0.11	1.02	0.72	1.01	1.05	1.07	0.66	0.58	0.086	0.29	0.11	0.18	1.26	0.98	0.54	1.19
Er	0.21	0.17	0.48	0.38	1.08	2.09	2.84	2.91	3.08	1.90	1.71	0.27	0.82	0.35	0.50	3.54	2.57	2.58	3.24
Tm	0.031	0.030	0.083	0.069	0.37	0.29	0.44	0.44	0.49	0.32	0.30	0.042	0.12	0.047	0.073	0.57	0.39	0.29	0.51

Table 2. Cont.

Sample No.	NCN01 02-ls1	NCN01 02-Di1	NCN01 04-grt2	NCN-PM01- b09	NCN01 05-ss1	NCN01 05-hl3	NCN02 10- $\gamma\pi$ 1	NCN02 10- $\gamma\pi$ 1(1)	NCN02 10- $\gamma\pi$ 3	NCN02 12-r $\pi$ 1	NCN02 12- $\gamma\pi$ 2	NCN01 13-Sph1	NCN- Zn1	NCN01 14-ls1	NCN01 17-Di1	NCN03 05-Ms2	NCN01 20-SK1	NCN01 20-ss1	NCN02 19- $\gamma\pi$ 1
Sample Name	ls	Px SK	Grt-Px SK	Grt-Px SK	ss	SK hl	$\gamma\pi$	$\gamma\pi$	$\gamma\pi$	$\gamma\pi$	$\gamma\pi$	Sph SK	Sph SK	ls	Grt-Px SK	Ms -Grt-Px SK	SK ss	ss	$\gamma\pi$
Zone	1	2	3	3	4	4	5	5	5	5	5	9	11	12	13	14	15	16	19
Yb	0.21	0.19	0.57	0.45	2.9	1.95	2.78	2.86	3.07	2.18	2.06	0.28	0.82	0.32	0.46	3.61	2.32	1.3	3.28
Lu	0.032	0.031	0.080	0.079	0.41	0.29	0.41	0.44	0.47	0.36	0.32	0.039	0.13	0.047	0.072	0.53	0.36	0.25	0.49
Hf	0.058	0.37	0.15	0.3	8.72	3.97	4.6	4.3	4.3	2.2	2.5	0.21	2.0	0.087	0.29	4.62	5.75	12.58	1.34
Ta	0.013	0.092	0.096	0.11	0.82	0.64	0.90	0.41	1.08	1.02	1.00	0.14	0.20	0.027	0.088	1.15	0.74	1.9	2.36
Pb	2.94	86.4	60.3	193.350	36.1	58.4	34.64	48.42	18.21	14.87	9.39	5459	26340	3.97	1894	6.00	5.07	20.3	25.06
Th	0.23	0.56	0.43	1.0	23.6	7.46	18.19	19.51	20.55	22.45	21.06	0.51	1.98	0.40	0.73	17.9	10.37	11.4	3.89
U	1.25	0.67	0.99	0.91	0.98	1.84	2.38	3.79	2.54	2.95	2.95	0.45	1.80	0.20	0.78	8.43	2.40	2.14	782.9
$\Sigma$ REE	8.55	9.05	8.24	11.57	115.47	144.71	221.09	231.19	245.25	185.74	135.37	5.77	46.55	10.68	18.86	123.47	237.56	192.45	271.29
La <sub>N</sub> /Yb <sub>N</sub>	7.51	7.14	1.85	5.50	9.48	10.74	11.22	11.94	12.20	15.07	11.09	2.28	8.15	5.98	5.29	3.87	14.75	3.68	12.71
$\delta$ Eu	0.72	0.59	1.02	0.48	0.78	0.96	0.40	0.42	0.44	0.69	0.54	0.19	0.83	0.76	0.77	0.48	1.16	0.68	0.43
$\delta$ Ce	0.66	1.00	0.70	0.56	1.02	1.02	1.07	1.05	1.05	1.04	1.05	0.77	0.89	0.59	0.91	1.03	1.03	4.07	1.03

Notes: Px SK: Pyroxene skarn; Grt-Px SK: Garnet-pyroxene skarn; Sph SK: Sphalerite-bearing skarn; Ms-Grt-Px SK: Muscovite-garnet-pyroxene skarn;  $\gamma\pi$ : granite porphyry; ls: limestone; ss: sandstone; SK ss: Skarnified sandstone; SK hfl: Skarnified hornfels. Oxides and LOI in wt.%, trace elements in ppm.

**Table 3.** Results of mass-change calculations of altered rocks from the Nuocang deposit, western Gangdese.

Zone	2	3	3	9	11	13	4	14	15
Sample No.	NCN0102-Di1	NCN0104-grt2	NCN-PM01-b09	NCN0113-Sph1	NCN-Zn1	NCN0117-Di1	NCN0105-hl3	NCN0305-MS2	NCN0120-SK1
Rock Type	Px SK	Grt-Px SK	Grt-Px SK	Sph SK	Sph SK	Grt-Px SK	Skarnified	Ms-Grt-Px SK	SK ss
SiO <sub>2</sub>	26.29	9.80	19.23	15.55	5.00	2.72	−55.51	−61.18	−57.43
TiO <sub>2</sub>	0.00	−0.01	0.00	−0.01	0.04	−0.01	0.10	−0.24	0.25
Fe <sub>2</sub> O <sub>3</sub> <sup>T</sup>	14.84	6.03	9.54	4.72	2.58	2.34	0.28	0.25	1.85
MnO	1.35	0.45	1.03	0.69	0.29	0.04	0.06	0.07	0.26
MgO	0.01	−0.13	−0.16	−0.39	−0.26	−0.43	−0.07	−0.16	0.59
CaO	−40.84	−47.04	−43.31	−48.70	−50.55	−50.40	7.66	7.81	12.44
Na <sub>2</sub> O	0.01	−0.01	0.01	0.01	−0.01	−0.03	−1.36	−1.38	−1.38
K <sub>2</sub> O	−0.06	−0.08	−0.07	−0.08	−0.07	−0.08	−2.27	−3.12	−3.67
P <sub>2</sub> O <sub>5</sub>	−0.02	−0.02	−0.02	−0.02	−0.02	−0.02	0.09	−0.05	0.16
Rb	−1.88	−3.05	−1.94	−3.92	−2.99	−4.00	−788.25	−852.98	−885.12
Sr	−847.66	−855.50	−843.73	−860.13	−833.38	−858.12	158.06	197.36	343.66
Ba	−7.81	−8.22	9.52	−10.77	1.36	−10.61	−145.84	−188.33	−224.94
Li	0.23	−1.44	0.32	1.68	−0.72	−1.95	−19.07	−18.81	−6.44
Zr	5.12	−1.68	1.85	−0.67	6.16	−1.91	−274.69	−300.59	−223.72
Hf	0.14	−0.03	0.07	−0.01	0.27	−0.04	−8.53	−8.60	−7.25
Nb	0.14	−0.04	0.70	−0.04	0.07	−0.14	1.31	0.14	3.36
Ta	0.03	0.01	0.03	0.02	0.01	−0.01	−1.02	−0.85	−0.92
Th	0.01	−0.20	0.12	−0.17	0.03	−0.23	−13.51	−9.56	−11.36
U	−0.33	−0.45	−0.32	−0.60	−0.41	−0.63	−0.58	2.18	−0.14
Pb	47.76	13.14	83.30	1593.85	4555.96	219.95	2.98	−25.54	−25.20
Zn	189.87	36.96	141.73	976.72	5916.94	22.97	16.83	−40.80	−16.06
Cu	−2.21	−1.29	4.93	−1.62	0.81	−2.64	−14.89	−16.08	−14.64
Sn	189.87	36.96	141.73	976.72	5916.94	22.97	16.83	−40.80	−16.06

Notes: Px SK: Pyroxene skarn; Grt-Px SK: Garnet-pyroxene skarn; Sph SK: Sphalerite-bearing skarn; Ms-Grt-Px SK: Muscovite-garnet-pyroxene skarn; γπ: granite porphyry; ls: limestone; ss: sandstone; SK ss: Skarnified sandstone; SK hfl: Skarnified hornfels.

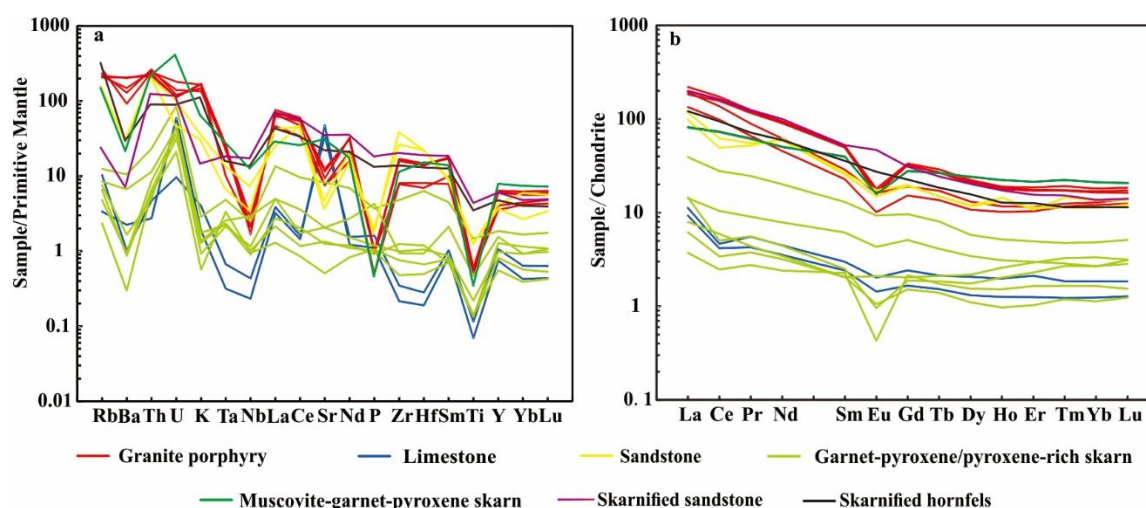


**Figure 6.** Primitive mantle-normalized trace elements (a) and chondrite-normalized REE, (b) patterns for the skarn, limestone, sandstone, skarnified hornfels and sandstone, granite porphyry, and rhyolite in the Nuocang Pb-Zn polymetallic deposit. Data sources: Trace elements of the granite porphyry and rhyolite are from Jiang et al. [19].

## 6.2. Skarn Mineralogy

### 6.2.1. Pyroxene

Pyroxene, as the most abundant skarn mineral in Nuocang, widely occurs in both the endoskarn and exoskarn. According to the mineral assemblages and spatial distribution characteristics, two types of pyroxenes have been identified: pyroxene I (average  $\text{Di}_{3.0}\text{Hd}_{87.3}\text{Jo}_{9.7}$ ) is more Fe-rich, and mostly occurs in the distal zones (zones 2, 9, 11, and 13; Table 4; Figure 7a). It occurs in dark green coloured, long prismatic, euhedral-subhedral crystals, and usually coexists with or cuts through the euhedral, coarse garnet aggregates (Figures 3e–g and 4d). Locally, ilvaite, magnetite, actinolite together with quartz and calcite replaced these pyroxenes (Figures 3e and 4e,h). Disseminated galena and sphalerite, occur within the pyroxene I aggregates (Figures 3i and 4e). In contrast, pyroxene II (average  $\text{Di}_{17.7}\text{Hd}_{68.6}\text{Jo}_{13.7}$ ) formed in proximal locations within the skarnified sandstone or volcanic rocks, which is enriched in magnesium and manganese (Figure 7a). It commonly occurs as dark green, anhedral-subhedral, granular or radial shaped, which forms massive aggregates (Figure 7b). In rare cases, pyroxene can be replaced by subhedral-euhedral anisotropic garnet (Figure 4f), associated with calcite, quartz, and minor plagioclase, chlorite, pyrite and chalcocopyrite. Pyroxene II exhibits zoning, showing a pale to dark colour, corresponding to a decreasing content of Hd but increasing content of Di and Jo from the core to rim (Figure 7b).

**Table 4.** Summary of electron probe microanalytical data for pyroxene (wt.%) in the Nuocang deposit, western Gangdese.

Sample No.	PM01-b08	PM01-b09	PM01-B13	0117-Di2				NCNPM01-b15-2				NCN0120-Tr1				NCN0119-Grt2				
Type	I								II											
					Core				Rim				Core				Rim			
SiO <sub>2</sub>	49.15	48.85	49.27	49.20	48.91	48.74	49.21	48.41	48.70	48.37	50.65	50.80	50.53	51.21	50.10	50.30	50.03			
TiO <sub>2</sub>	0.00	0.00	0.00	0.00	0.00	0.00	0.00	0.00	0.00	0.00	0.00	0.00	0.00	0.00	0.00	0.00	0.00	0.00		
Al <sub>2</sub> O <sub>3</sub>	0.03	0.05	0.02	0.02	0.06	0.23	0.00	0.06	0.10	0.14	0.08	0.06	0.10	0.09	0.02	0.06	0.05			
Cr <sub>2</sub> O <sub>3</sub>	0.00	0.00	0.01	0.00	0.00	0.00	0.02	0.00	0.00	0.02	0.00	0.00	0.00	0.02	0.00	0.00	0.03			
FeO	24.37	24.49	22.55	24.33	26.25	25.24	24.85	24.64	24.63	23.11	18.42	15.05	17.97	14.25	19.87	19.65	20.37			
MnO	2.30	3.42	1.97	1.83	2.06	2.48	2.21	2.92	2.83	4.96	2.42	5.00	3.80	4.38	3.13	4.02	1.78			
MgO	1.13	0.42	2.26	1.53	0.12	0.37	0.91	0.38	0.54	0.04	4.64	5.15	4.26	5.96	3.45	3.00	3.96			
CaO	22.95	22.63	22.91	23.03	23.15	23.09	23.45	23.07	23.38	22.93	23.77	23.91	23.33	23.63	23.53	23.28	23.44			
Na <sub>2</sub> O	0.06	0.04	0.01	0.06	0.07	0.07	0.03	0.02	0.04	0.05	0.03	0.00	0.06	0.03	0.01	0.04	0.06			
Total	99.98	99.91	99.09	99.99	100.62	100.22	100.68	99.5	100.22	99.62	100.01	99.97	100.05	99.57	100.11	100.35	99.72			
Citations based on 6 oxygens																				
Si	2.023	2.015	2.043	2.023	1.991	2.000	2.010	2.003	1.999	1.996	2.071	2.077	2.067	2.099	2.052	2.056	2.055			
Ti	0.000	0.000	0.000	0.000	0.000	0.000	0.000	0.000	0.000	0.000	0.000	0.000	0.000	0.000	0.000	0.000	0.000			
Al	0.002	0.003	0.001	0.001	0.003	0.011	0.000	0.003	0.005	0.007	0.004	0.003	0.005	0.004	0.001	0.003	0.002			
Cr	0.000	0.000	0.000	0.000	0.000	0.000	0.001	0.000	0.000	0.001	0.000	0.000	0.000	0.000	0.000	0.000	0.001			
Fe <sup>3+</sup>	0.000	0.000	0.000	0.000	0.019	0.000	0.000	0.000	0.001	0.005	0.000	0.000	0.000	0.000	0.000	0.000	0.000			
Fe <sup>2+</sup>	0.839	0.845	0.782	0.837	0.894	0.866	0.849	0.853	0.845	0.798	0.630	0.515	0.615	0.489	0.681	0.672	0.700			
Mn	0.080	0.119	0.069	0.064	0.071	0.086	0.076	0.102	0.098	0.173	0.084	0.173	0.132	0.152	0.109	0.139	0.062			
Mg	0.041	0.015	0.083	0.055	0.004	0.014	0.033	0.014	0.020	0.001	0.168	0.186	0.154	0.216	0.125	0.108	0.144			
Ca	1.012	1.000	1.018	1.015	1.010	1.015	1.026	1.023	1.028	1.014	1.042	1.047	1.023	1.038	1.032	1.019	1.032			
Na	0.004	0.003	0.001	0.005	0.005	0.006	0.002	0.002	0.003	0.004	0.002	0.000	0.005	0.002	0.001	0.003	0.005			
Mole percentage																				
Di	4.26	1.56	8.88	5.80	0.44	1.40	3.43	1.44	2.05	0.14	19.02	21.29	17.09	25.21	13.66	11.79	15.86			
Hd	87.40	86.25	83.72	87.53	92.37	89.68	88.60	87.98	87.75	82.12	71.47	58.90	68.30	57.03	74.46	73.08	77.30			
Jo	8.34	12.19	7.41	6.67	7.19	8.92	7.97	10.57	10.20	17.73	9.51	19.81	14.61	17.76	11.88	15.13	6.84			

Note: Di—Diopside, Hd—Hedenbergite, Joh—Johannsenite.

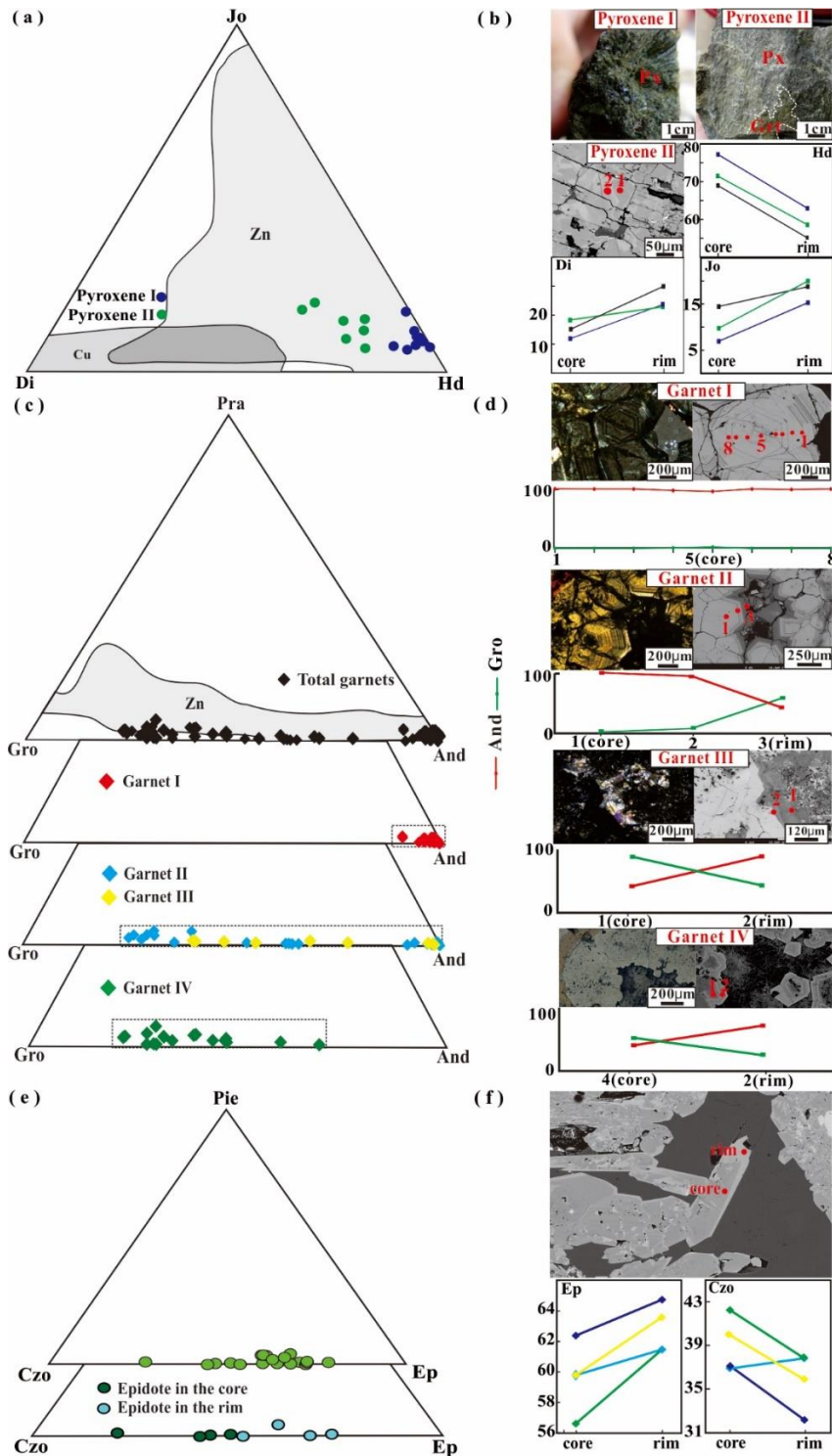


**Figure 7.** (a) Ternary diagrams showing compositional variation in pyroxene, expressed in relative proportions of diopside (Di), hedenbergite (Hd), and johannsenite (Jo) endmembers; (b) Composition variation of hedenbergite and diopside from the type II pyroxenes zoning in the Nuocang deposit and corresponding photographs; (c) Ternary diagrams showing compositional variation (EPMA data) in garnet, expressed in relative proportions of andradite (And), grossular (Gro) and pyrospite (Pra) endmembers; (d) Composition variation of andradite and grossular from the type I, II, III garnets zoning in the Nuocang deposit and corresponding photographs; (e) Ternary plots of epidote-clinozoisite series compositions from the Nuocang deposit; (f) Composition variation of epidote and clinozoisite from the core to the rim in the Nuocang deposit and corresponding photographs.

### 6.2.2. Garnet

In contrast with the widely developed pyroxene in the skarn, garnet usually occurs as crumbly aggregates in the pyroxene-rich skarn (Figure 3c,e), with minor garnet associated with pyroxene or epidote cutting through the hornfels or replacing the granite porphyry (Figure 3b,d). Four types of garnets could be recognized based on the textural and structural features under the optical polarizing microscope: (1) Garnet I chiefly occurs in the exoskarn. It is generally dark brown, brown, or dark green, euhedral-subhedral, coarse grained, displaying the isotropic characteristics and pronounced growth zoning (Figures 4b and 7d). Generally, garnet I is dominantly andradite ( $\text{And}_{90}\text{Gro}_8$  to  $\text{And}_{100}\text{Gro}_0$ ), with almost unchanged chemical composition from core to rim (Table 5; Figure 7c,d). These garnets usually form aggregates in the skarn, however, with no obvious alterations and mineralization; (2) garnet II commonly occurs in the rim of garnet I aggregates, in medium to coarse grained euhedral to subhedral aggregates with conspicuous oscillatory zonings, with isotropic core and anisotropic rim.

These garnets have a wide variation of compositions from the core to rim, ranging from  $\text{And}_{98}\text{Gro}_{0.2}$  to  $\text{And}_{26}\text{Gro}_{72}$  (Table 4; Figure 7c,d). In comparison with garnet I, garnet II was moderately affected by the later hydrothermal fluid, where it occurs with later pyroxene, ilvaite, quartz, and calcite (Figures 4c and 7d); (3) Garnet III is also intergrown with garnet I and II (Figure 4d). However, it is characterized by fine to medium grained, anhedral crystals. It generally shows anisotropic core, and isotropic rim (Figure 7d). The anhedral garnet III shows high grossular endmember compositions in the core but low grossular endmember compositions in the rim ( $\text{And}_{41}\text{Gro}_{58}$  to  $\text{And}_{99.9}\text{Gro}_0$ ) (Figure 7c,d); (4) Garnet IV is obviously different from garnet I, II, and III that are mainly located in the endoskarn. Commonly they show the yellow green, irregular fine to medium-grained, and anisotropic characteristics.

Garnet IV shows a relatively higher grossular end-member composition ( $\text{And}_{23}\text{Gro}_{75}$  to  $\text{And}_{61}\text{Gro}_{38}$ ) than others (Figure 7c) and displays a decreasing trend of grossular endmember compositions and an increasing andradite component from the core to rim (Figure 7d). Garnet IV tends to be isolated in the interstices of pyroxene aggregates, replacing the pyroxene (Figure 7d), or cutting through the garnet I aggregates (Figure 7b,d), suggesting it formed later than that of garnet I, II, and III.

### 6.2.3. Epidote

Though the retrograde minerals are scarce when compared to the prograde minerals, epidote is very common in the retrograde stage. It predominantly is exhibited as euhedral, columnar crystals, replacing garnet and was replaced by chlorite, muscovite, quartz, and calcite (Figures 3g and 4i). The epidote has a relatively narrow range of  $\text{SiO}_2$  (37.63–39.33 wt.%) and  $\text{CaO}$  (22.93–23.99 wt.%), but wider variations of  $\text{Al}_2\text{O}_3$  (23.10–28.67 wt.%), and  $\text{FeO}$  (5.16–11.66 wt.%) values, with a range of compositions ( $\text{Ep}_{28.7-74.6}\text{Czo}_{24.4-70.2}\text{Pie}_{0.2-4}$ ) and relatively low  $\text{Fe}/(\text{Fe} + \text{Al})$  values of 0.10–0.23 (mean of 0.19). Interestingly, the typical zoning phenomenon could be identified in some epidotes (Table 6; Figure 7e), yielding dark green colour in the core ( $\text{Ep}_{42.5}\text{Czo}_{56.8}\text{Pie}_{0.7}$ ) and pale green in the rim ( $\text{Ep}_{61.3}\text{Czo}_{37.5}\text{Pie}_{1.2}$ ; Figure 7f), indicating it formed in a relatively turbulent environment.



Table 5. Cont.

Sample No.	NCN0115-Gr1										NCNPM01-b08										NCN0304-Gr1										NCN0417-Gr1									
Type	I					II					Core to rim					Rim to core					Rim to core					Rim to core														
	Rim to core		Rim to core, to rim			Core to rim					Core to rim					Rim to core					Rim to core					Rim to core														
SiO <sub>2</sub>	35.26	35.22	37.80	36.31	35.02	36.22	37.94	37.00	34.73	36.29	34.75	36.46	38.12	38.36	35.06	37.61	37.39	35.24	35.20	38.36	35.37	38.05	35.14	35.16																
TiO <sub>2</sub>	0.00	0.00	0.01	0.00	0.00	0.00	0.06	0.05	0.03	0.35	0.02	0.00	0.00	0.00	0.00	0.09	0.00	0.00	0.00	0.07	0.00	0.36	0.00	0.00																
Al <sub>2</sub> O <sub>3</sub>	0.28	0.27	16.10	7.94	0.51	7.56	15.57	9.85	0.71	7.02	0.47	7.77	15.43	16.07	1.69	13.96	13.48	1.40	0.31	16.91	0.12	16.85	0.35	0.26																
Cr <sub>2</sub> O <sub>3</sub>	0.00	0.02	0.03	0.03	0.00	0.00	0.00	0.00	0.05	0.00	0.00	0.00	0.00	0.00	0.00	0.02	0.00	0.00	0.00	0.00	0.00	0.04	0.00	0.01																
Fe <sub>2</sub> O <sub>3</sub>	30.95	30.74	9.50	20.64	30.46	20.96	10.07	17.38	29.71	20.86	30.59	20.80	10.31	9.82	28.70	12.08	13.11	29.35	30.87	8.82	31.05	8.42	30.48	30.50																
MnO	0.13	0.11	0.56	0.46	0.32	0.45	1.26	0.57	0.34	0.42	0.34	0.50	0.92	0.49	0.30	0.60	1.45	0.53	0.50	0.53	0.54	0.62	0.61	0.58																
MgO	0.01	0.02	0.00	0.01	0.02	0.00	0.00	0.00	0.02	0.02	0.05	0.00	0.00	0.00	0.02	0.00	0.04	0.08	0.08	0.00	0.06	0.02	0.03	0.09																
CaO	33.67	33.39	35.83	34.60	33.31	34.59	34.67	34.88	33.45	34.66	33.24	34.36	35.15	35.59	33.55	35.26	34.55	33.24	32.74	35.96	33.24	35.82	32.82	33.24																
Na <sub>2</sub> O	0.00	0.00	0.00	0.00	0.00	0.00	0.00	0.00	0.02	0.00	0.00	0.00	0.00	0.02	0.00	0.00	0.00	0.02	0.00	0.00	0.02	0.03	0.02	0.02																
Total	100.30	99.77	99.82	100.00	99.63	99.78	99.57	99.72	99.06	99.62	99.45	99.88	99.92	100.35	99.31	99.59	99.99	99.80	99.72	100.66	100.39	100.21	99.44	99.85																
	Cations based on 12 oxygens																																							
Si	2.966	2.979	2.939	2.943	2.963	2.945	2.971	2.972	2.949	2.961	2.948	2.961	2.974	2.972	2.957	2.964	2.949	2.964	2.983	2.951	2.976	2.940	2.983	2.972																
Ti	0.000	0.000	0.001	0.000	0.000	0.000	0.004	0.003	0.002	0.021	0.001	0.000	0.000	0.000	0.000	0.005	0.000	0.000	0.000	0.004	0.000	0.021	0.000	0.000																
Al	0.028	0.027	1.475	0.759	0.050	0.724	1.437	0.932	0.071	0.675	0.047	0.743	1.419	1.467	0.167	1.297	1.253	0.139	0.031	1.533	0.012	1.535	0.035	0.025																
Cr	0.000	0.001	0.002	0.002	0.000	0.000	0.000	0.000	0.003	0.000	0.000	0.000	0.000	0.000	0.000	0.001	0.000	0.000	0.000	0.000	0.000	0.003	0.000	0.001																
Fe <sup>3+</sup>	1.960	1.957	0.556	1.259	1.940	1.283	0.593	1.050	1.899	1.281	1.953	1.271	0.605	0.573	1.822	0.717	0.778	1.859	1.968	0.511	1.967	0.490	1.947	1.940																
Fe <sup>2+</sup>	0.000	0.000	0.000	0.000	0.000	0.000	0.000	0.000	0.000	0.000	0.000	0.000	0.000	0.000	0.000	0.000	0.000	0.000	0.000	0.000	0.000	0.000	0.000	0.000																
Mn	0.009	0.008	0.037	0.032	0.023	0.031	0.084	0.039	0.024	0.029	0.024	0.034	0.060	0.032	0.021	0.040	0.097	0.038	0.036	0.035	0.038	0.041	0.044	0.042																
Mg	0.001	0.001	0.000	0.001	0.002	0.000	0.000	0.000	0.001	0.001	0.004	0.000	0.000	0.000	0.001	0.000	0.000	0.003	0.006	0.000	0.004	0.002	0.002	0.006																
Ca	3.034	3.026	2.986	3.005	3.019	3.013	2.908	3.002	3.044	3.029	3.021	2.990	2.937	2.954	3.031	2.977	2.919	2.996	2.972	2.964	2.998	2.966	2.985	3.009																
Na	0.000	0.000	0.000	0.000	0.000	0.000	0.000	0.000	0.004	0.000	0.000	0.000	0.000	0.002	0.000	0.000	0.000	0.000	0.003	0.000	0.003	0.004	0.003	0.003																
	Mole percentage																																							
Ura	0.00	0.07	0.08	0.09	0.00	0.00	0.00	0.00	0.16	0.00	0.00	0.00	0.00	0.00	0.00	0.05	0.00	0.00	0.00	0.00	0.00	0.13	0.00	0.04																
And	98.60	98.58	27.36	62.35	97.47	63.91	29.23	52.98	96.24	65.48	97.65	63.11	29.90	28.08	91.58	35.59	38.29	93.04	98.44	24.99	99.42	24.15	98.26	98.67																
Pyr	0.02	0.05	0.00	0.02	0.06	0.00	0.00	0.00	0.04	0.05	0.13	0.00	0.00	0.00	0.04	0.00	0.00	0.09	0.20	0.00	0.15	0.05	0.08	0.22																
Spe	0.32	0.27	1.20	1.05	0.76	1.04	2.75	1.30	0.81	0.99	0.81	1.13	1.99	1.06	0.71	1.32	3.18	1.26	1.19	1.13	0.44	1.33	1.47	1.07																
Gro	1.06	1.03	70.46	36.49	1.71	35.05	66.28	45.72	2.74	33.48	1.40	35.76	66.87	68.48	7.67	62.99	57.43	5.61	0.17	71.68	0.00	73.26	0.19	0.00																
Alm	0.00	0.00	0.90	0.00	0.00	0.00	1.74	0.00	0.00	0.00	0.00	0.00	1.25	2.38	0.00	0.10	1.06	0.00	0.00	2.20	0.00	1.07	0.00	0.00																

Table 5. Cont.

Sample No.	NCN0113-Grt1				NCN0117-Di1				NCNPM01-b09				NCNPM01-b15-2				NCN0118-Grt1				NCN0119-Grt1						
Type	III				IV																						
	Rim to core	Core to Rim	Rim to core	Core to rim	Core to rim	Core to rim	Core to rim	Core to rim	Core to rim	Core to rim	Core to rim	Core to rim	Core to rim	Core to rim													
SiO <sub>2</sub>	36.37	36.55	37.78	35.56	37.26	36.66	36.69	34.98	35.14	36.88	37.41	37.08	36.38	35.66	36.06	35.62	37.47	37.50	38.67	37.55	38.63	37.9	38.28	37.99	37.83	37.32	35.64
TiO <sub>2</sub>	0.05	0.11	0.08	0.00	0.01	0.37	0.02	0.00	0.00	0.64	0.25	0.34	0.07	0.012	0.01	0.08	0.02	0.84	0.33	0.51	0.26	0.13	0.00	0.06	0.93	0.50	0.76
Al <sub>2</sub> O <sub>3</sub>	4.34	6.52	11.52	0.34	12.85	9.09	12.76	0.10	0.00	13.13	13.85	12.59	14.24	14.13	13.16	6.08	11.11	16.52	15.07	14.38	17.16	14.55	11.55	8.36	15.69	14.60	10.87
Cr <sub>2</sub> O <sub>3</sub>	0.02	0.01	0.00	0.01	0.01	0.00	0.01	0.00	0.02	0.00	0.00	0.00	0.01	0	0	0.00	0.02	0.01	0.00	0.00	0	0.01	0	0.01	0.02	0.00	0.00
Fe <sub>2</sub> O <sub>3</sub>	25.09	22.94	15.50	31.10	13.77	18.25	14.11	30.87	31.70	12.23	12.64	14.27	9.22	9.10	10.22	22.82	15.77	7.76	10.06	10.81	7.93	12.24	16.32	20.47	9.53	10.92	15.80
MnO	0.21	0.19	0.43	0.16	0.38	0.26	0.45	0.15	0.13	1.53	1.51	0.86	0.34	0.35	0.29	0.29	0.97	1.26	2.14	1.21	1.18	0.83	0.84	0.59	1.58	1.26	0.58
MgO	0.03	0.00	0	0.04	0.00	0.02	0.00	0.01	0.00	0.00	0.00	0.00	0.01	0	0.01	0.00	0.02	0.04	0.06	0.02	0.04	0.00	0.01	0.03	0.06	0.02	0.01
CaO	34.30	34.55	35.22	33.59	35.32	35.03	35.61	33.08	33.65	34.29	33.92	34.07	31.12	30.66	30.49	34.37	35.28	35.92	34.38	35.68	34.92	34.45	34.11	33.68	34.08	35.03	34.50
Na <sub>2</sub> O	0.02	0.03	0.00	0.00	0.00	0.00	0.00	0.00	0.00	0.00	0.00	0.00	0.00	0.00	0.00	0	0.01	0	0	0.01	0	0	0	0	0.00	0.00	0.00
Total	100.43	100.89	100.53	100.80	99.61	99.68	99.65	99.19	100.63	98.71	99.59	99.21	91.39	89.912	90.24	99.25	100.70	99.88	100.72	100.27	100.13	100.11	101.11	101.18	99.73	99.65	98.16
Cations based on 12 oxygens																											
Si	2.985	2.958	2.986	2.977	2.952	2.957	2.908	2.978	2.954	2.918	2.931	2.927	2.938	3.103	3.090	2.935	2.963	2.911	3.005	2.934	2.987	2.973	3.019	3.042	2.964	2.934	2.898
Ti	0.003	0.006	0.005	0.000	0.001	0.022	0.001	0.000	0.000	0.038	0.015	0.020	0.010	0.004	0.001	0.005	0.001	0.049	0.019	0.030	0.015	0.008	0.000	0.003	0.055	0.030	0.046
Al	0.420	0.622	1.073	0.034	1.200	0.864	1.192	0.010	0.000	1.225	1.279	1.171	1.324	1.431	1.443	0.590	1.035	1.512	1.380	1.325	1.564	1.345	1.074	0.789	1.449	1.353	1.042
Cr	0.001	0.001	0.000	0.001	0.001	0.000	0.001	0.000	0.002	0.000	0.000	0.000	0.000	0.001	0.000	0.000	0.001	0.001	0.000	0.000	0.000	0.000	0.000	0.001	0.001	0.000	0.000
Fe <sup>3+</sup>	1.550	1.397	0.005	0.000	0.821	1.108	0.842	1.978	2.006	0.810	0.828	0.942	0.592	0.594	0.668	1.416	0.939	0.453	0.572	0.636	0.462	0.723	0.969	1.234	0.562	0.646	0.967
Fe <sup>2+</sup>	0.000	0.000	0.000	0.000	0.000	0.000	0.000	0.000	0.000	0.000	0.000	0.000	0.000	0.000	0.000	0.000	0.000	0.000	0.017	0.000	0.000	0.000	0.000	0.000	0.000	0.000	0.000
Mn	0.015	0.013	0.028	0.011	0.025	0.018	0.030	0.010	0.009	0.103	0.100	0.058	0.026	0.025	0.026	0.020	0.065	0.083	0.141	0.080	0.078	0.055	0.056	0.040	0.105	0.084	0.040
Mg	0.002	0.000	0.000	0.003	0.000	0.002	0.000	0.001	0.000	0.000	0.000	0.000	0.001	0.001	0.000	0.000	0.001	0.003	0.004	0.001	0.003	0.000	0.000	0.002	0.004	0.001	0.000
Ca	3.016	2.996	2.982	3.013	2.998	3.028	3.025	3.017	3.030	2.907	2.847	2.882	3.050	2.843	2.847	3.034	2.989	2.987	2.862	2.987	2.893	2.895	2.882	2.889	2.860	2.951	3.006
Na	0.003	0.004	0.000	0.000	0.000	0.000	0.000	0.000	0.000	0.000	0.000	0.000	0.000	0.000	0.000	0.000	0.002	0.000	0.000	0.002	0.000	0.000	0.000	0.000	0.000	0.000	0.000
Mole percentage																											
Ura	0.07	0.03	0.00	0.04	0.04	0.00	0.03	0.00	0.08	0.00	0.00	0.00	0.00	0.00	0.00	0.00	0.05	0.04	0.00	0.00	0.00	0.00	0.00	0.06	0.00	0.00	0.00
And	78.62	69.17	48.38	98.22	40.61	56.19	41.38	99.46	99.92	39.80	39.32	44.57	30.89	29.32	31.63	70.57	47.54	23.07	29.14	32.43	22.80	34.96	47.44	60.99	27.94	32.32	48.14
Pyr	0.08	0.00	0.00	0.09	0.00	0.06	0.00	0.03	0.00	0.00	0.00	0.00	0.03	0.03	0.00	0.00	0.04	0.09	0.13	0.04	0.10	0.01	0.01	0.06	0.14	0.05	0.02
Spe	0.50	0.42	0.96	0.39	0.84	0.59	0.98	0.35	0.00	3.37	3.17	1.82	0.90	0.81	0.81	0.68	2.20	2.80	4.79	2.72	2.55	1.77	1.82	1.32	3.47	2.80	1.33
Gro	20.73	29.67	50.66	1.25	58.21	43.16	57.61	0.16	0.00	56.83	57.51	53.60	68.17	69.84	67.56	28.75	50.18	74.01	65.38	64.81	74.56	63.26	50.72	37.62	68.38	64.83	50.51
Alm	0.00	0.72	0.00	0.00	0.30	0.00	0.00	0.00	0.00	0.00	0.00	0.00	0.00	0.00	0.00	0.00	0.00	0.00	0.56	0.00	0.00	0.00	0.00	0.00	0.00	0.00	0.00

Note: And—andradite, Gro—grossular, Alm—almandine, Pyr—pyrope, Spe—spessartine, Ura—uvarovite.

**Table 6.** Summary of electron probe microanalytical data for epidote (wt.%) in the Nuocang deposit, western Gangdese

Sample No.	NCN-SK4	PM01-b01	NCN0102-Ep1	PM01-B13	NCN0305-MS2						NCN0119-Ep1			NCN0120-Sk1						
					Rim	Core	Core	Rim	Rim	Core	Core	Rim								
SiO <sub>2</sub>	38.59	37.63	38.50	38.31	37.94	38.14	38.28	38.04	38.27	38.76	38.44	38.82	38.76	39.06	39.06	39.33	38.41	38.33	38.74	38.82
TiO <sub>2</sub>	0.06	0.03	0.02	0.06	0.00	0.09	0.00	0.00	0.04	0.03	0.02	0.02	0.00	0.00	0.02	0.04	0.03	0.10	0.14	0.02
Al <sub>2</sub> O <sub>3</sub>	24.71	25.27	25.19	25.59	24.78	23.73	25.59	23.10	24.11	27.11	24.98	26.91	25.28	25.82	27.02	28.67	23.36	24.62	24.83	26.91
FeO	0.78	0.00	0.25	0.51	0.00	0.64	0.74	0.67	0.04	0.19	0.38	0.34	0.94	0.32	0.73	1.03	1.29	0.81	0.98	0.34
Fe <sub>2</sub> O <sub>3</sub>	10.12	11.33	10.26	9.64	11.43	11.26	9.39	12.21	11.41	7.63	10.70	8.36	9.58	8.52	7.26	4.59	10.26	10.34	9.82	8.36
MnO	0.12	0.16	0.08	0.09	0.03	0.19	0.52	0.14	0.12	0.09	0.60	0.12	0.50	0.04	0.03	0.17	0.06	0.39	0.28	0.12
MgO	0.02	0.02	0.00	0.00	0.00	0.00	0.00	0.00	0.00	0.00	0.00	0.00	0.00	0.16	0.08	0.04	0.00	0.10	0.12	0.00
CaO	23.56	23.42	23.73	23.43	23.76	23.30	22.94	23.23	23.82	23.98	23.31	23.83	23.21	23.99	23.83	23.80	23.21	23.08	23.06	23.83
K <sub>2</sub> O	0.00	0.00	0.00	0.00	0.00	0.00	0.00	0.00	0.00	0.00	0.00	0.00	0.00	0.00	0.00	0.00	0.00	0.09	0.00	0.00
Na <sub>2</sub> O	0.00	0.00	0.02	0.02	0.00	0.00	0.00	0.00	0.00	0.01	0.00	0.02	0.00	0.04	0.00	0.00	0.00	0.02	0.00	0.02
Total	97.96	97.84	98.05	97.65	97.94	97.35	97.46	97.39	97.81	97.83	98.41	98.44	98.26	97.96	98.04	97.68	96.63	97.77	98.08	98.44
Cations calculated on the basis of 12.5 oxygen atoms																				
Si	3.04	2.98	3.02	3.00	3.01	3.06	3.01	3.09	3.04	2.96	3.02	2.97	3.04	3.01	2.98	2.94	3.10	3.04	3.04	3.05
Ti	0.00	0.00	0.00	0.00	0.00	0.01	0.00	0.00	0.00	0.00	0.00	0.00	0.00	0.00	0.00	0.00	0.00	0.01	0.00	0.01
Al	2.30	2.36	2.33	2.36	2.31	2.25	2.37	2.21	2.26	2.44	2.32	2.43	2.33	2.35	2.43	2.52	2.22	2.30	2.30	2.30
Fe <sup>3+</sup>	0.60	0.69	0.61	0.57	0.70	0.68	0.56	0.73	0.68	0.45	0.63	0.49	0.57	0.50	0.43	0.27	0.62	0.62	0.55	0.58
Fe <sup>2+</sup>	0.05	0.00	0.02	0.03	0.00	0.04	0.05	0.05	0.00	0.01	0.02	0.02	0.06	0.02	0.05	0.07	0.09	0.05	0.03	0.07
Mn	0.01	0.01	0.01	0.01	0.00	0.01	0.03	0.01	0.01	0.01	0.04	0.01	0.03	0.00	0.00	0.01	0.00	0.03	0.03	0.02
Mg	0.00	0.00	0.00	0.00	0.00	0.00	0.00	0.00	0.00	0.00	0.00	0.00	0.00	0.01	0.01	0.00	0.00	0.01	0.03	0.01
Ca	1.99	1.99	1.99	1.97	2.02	2.00	1.93	2.02	2.03	1.96	1.96	1.96	1.95	1.98	1.95	1.90	2.01	1.96	1.92	1.95
K	0.00	0.00	0.00	0.00	0.00	0.00	0.00	0.00	0.00	0.00	0.00	0.00	0.00	0.00	0.00	0.00	0.00	0.00	0.02	0.01
Na	0.00	0.00	0.00	0.00	0.00	0.00	0.00	0.00	0.00	0.00	0.00	0.00	0.00	0.01	0.00	0.00	0.00	0.00	0.00	0.00
Mole percentage																				
Pie	0.82	1.04	0.56	0.61	0.21	1.30	3.49	0.94	0.81	0.58	3.99	0.76	3.38	0.28	0.22	1.16	0.44	2.66	3.51	1.92
Ep	62.03	67.29	61.94	58.32	69.26	69.07	56.54	74.62	69.23	46.49	63.50	50.22	57.89	52.81	44.69	28.65	65.36	62.75	56.97	60.11
Czo	37.15	31.67	37.51	41.07	30.53	29.63	39.97	24.44	29.96	52.93	32.51	49.02	38.73	46.91	55.10	70.20	34.21	34.59	39.52	37.97

Note: Ep—Epidote, Czo—Clinzoisite, Pie—Piemontite. H<sub>2</sub>O not calculated.

6.2.4. Ilvaite

Ilvaite is a rare though characteristic species of some mineralized skarn deposits. So far it has been discovered in the Pb–Zn, Fe, Au, and W–Sn skarn, such as the Makeng skarn Fe deposit (China), the Jinchanghe skarn Fe–Cu–Pb–Zn deposit in China, the skarn Pb–Zn deposit in the Rhodope Mountains (Bulgaria), the Hahaigang skarn W–Mo polymetallic deposit (China), and the Fortitude skarn Au deposit (America) [24–29]. Two types of ilvaites were identified in this deposit: (1) Ilvaite I is usually presenting as irregular anhedral grains, which are interstitial in the garnet-pyroxene skarn (Figure 3e). It replaced garnet and pyroxene and was replaced by galena-sphalerite, suggesting the order of garnet and pyroxene earlier than the ilvaite which is earlier than the galena and sphalerite; (2) Ilvaite II occurs as euhedral columnar crystals in garnet-pyroxene skarn, associated with the quartz-chalcopyrite-sphalerite assemblage, and sometimes it was replaced by calcite in residual patches (Figures 3f and 4j). Two types of ilvaites have been analyzed, and the corresponding results suggest that both are Mn-ilvaite (Figure 8; Table 7). They have similar contents of SiO<sub>2</sub>, MgO, and CaO, and different contents of MnO (average contents of type I ilvaite: 4.45%, and type II ilvaite: 5.92%), and FeO<sup>T</sup> (average contents of type I ilvaite: 48.1%, and type II ilvaite: 46.2%).

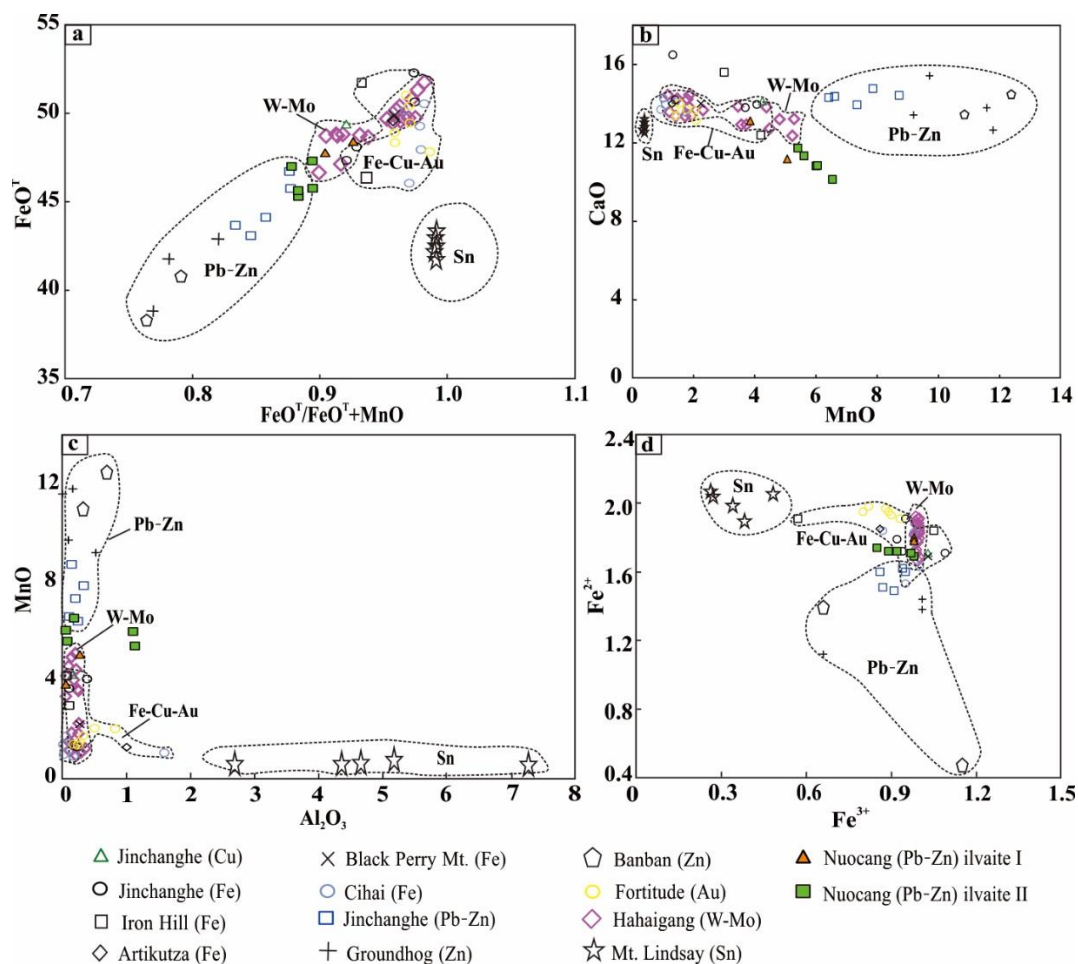


**Figure 8.** Binary plots of different major element ratios for ilvaite from the Nuocang skarn. (a) FeO<sup>T</sup> vs. FeO/(FeO<sup>T</sup> + MnO) diagram, (b) CaO vs. MnO diagram, (c) MnO vs. Al<sub>2</sub>O<sub>3</sub> diagram, (d) Fe<sup>2+</sup> vs. Fe<sup>3+</sup> diagram. Data sources: gold (Au) skarn [25]; Fe skarn [30–34]; Zn skarn [28,35]; Sn skarn [36]; Ilimaussaq complex [37]; W–Mo skarn, W–Mo (E) for early, first-generation ilvaite; W–Mo for late, second-generation ilvaite [25,28].

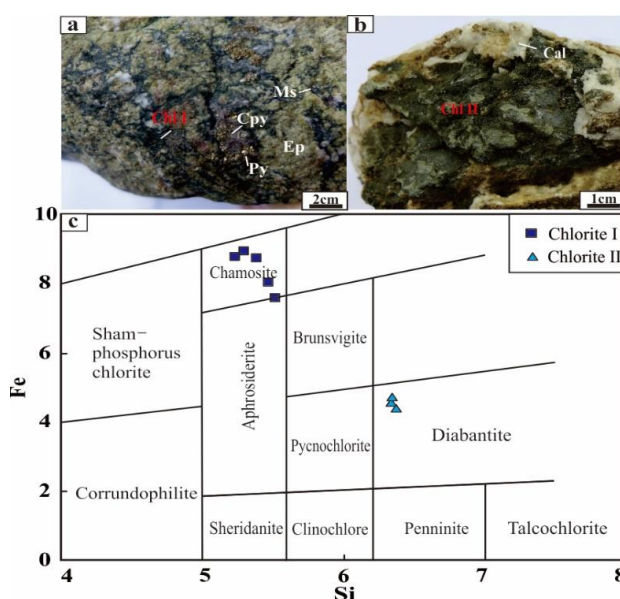
**Table 7.** Summary of electron probe microanalytical data for ilvaite (wt.%) in the Nuocang deposit, western Gangdese.

Sample No.	NCNPM01-b02-3				NCN0103-IIv1		
	Type	I				II	
SiO <sub>2</sub>	29.39	29.76	29.53	29.5	29.617	29.2	29.01
CaO	12.75	12.88	13.35	12.95	13.334	13.21	12.44
FeO	29.69	30.41	30.16	29.76	30.17	31.3	30.86
Fe <sub>2</sub> O <sub>3</sub>	19.22	16.55	17.33	17.63	19.05	19.01	18.79
ZnO	0.00	0.05	0.09	0.04	0.00	0.17	0.06
Al <sub>2</sub> O <sub>3</sub>	0.18	1.1	1.13	0.05	0.073	0.05	0.27
MgO	0.07	0.08	0.05	0.04	0.089	0.05	0.05
MnO	6.54	6.00	5.41	6.05	5.61	3.85	5.06
TFeO	46.98	45.30	45.76	45.63	47.30	48.41	47.77
Total	97.83	96.84	97.06	96.02	97.94	96.84	96.54
Fe/(Fe + Mg + Mn)	87.67	88.17	89.34	88.22	89.25	92.54	90.34
FeO <sup>T</sup> /FeO <sup>T</sup> + MnO	0.88	0.88	0.89	0.88	0.89	0.93	0.904

Note: H<sub>2</sub>O not calculated.

### 6.2.5. Chlorite

Chlorite is an important phase of hydrothermal alteration assemblages within the Nuocang deposit. It presents as fibrous and sheet aggregates that mainly occurred in the exoskarn near the limestone, with minor amounts in altered sandstone or volcanic rocks. Two types of chlorites have been identified in the Nuocang deposit: Chlorite I, forming in the late retrograde stage, is usually interstitial in epidote, associated with quartz, biotite or muscovite, minor pyrite and chalcopyrite (Figure 9a). Chlorite II always coexists with calcite. It was only discovered in the western part of the deposit, representing the post ore-stage of the quartz-calcite stage (Figure 9b). According to the classified method summarized by the Deer [38], the chlorite I, and II belong to chamosite and diabantite, respectively (Figure 9a–c). Representative EPMA data (Table 8) show low (Na<sub>2</sub>O + K<sub>2</sub>O + CaO) values < 0.5 wt.%, indicating the contamination-free chlorite compositions [39], highly variable Fe and Mg contents (FeO values of chlorite I: 22.43–24.37 wt.%, chlorite II: 38.25–44.26 wt.%; and MgO values of chlorite I: 22.43–44.26 wt.%, chlorite II: 0.27–16.05 wt.%) with a negative correlation. They have high Fe/(Fe + Mg) values of 0.57–0.99 that are indicative of forming in an Fe-rich environment [40]. They have relatively high Al/(Al + Mg + Fe) values of 0.36–0.40 (>0.35) and relatively low Mg/(Fe + Mg) values of 0.05–0.43, suggesting that they are similar to those from argillaceous protoliths [41].

**Figure 9.** (a) Type I chlorite; (b) type II chlorite; (c) Classification of type I, II chlorite composition.

**Table 8.** Summary of electron probe microanalytical data for chlorite (wt.%) in the Nuocang deposit, western Gangdese.

Sample No.	0102-Ep1		0305-Ms2		0417-Grt1		NCN0407-Ch11	
Type	I				II			
Chlorite								
SiO <sub>2</sub>	23.28	22.03	21.62	23.13	22.33	27.34	27.20	27.38
TiO <sub>2</sub>	0.00	0.00	0.00	0.02	0.05	0.00	0.00	0.02
Al <sub>2</sub> O <sub>3</sub>	19.55	19.43	19.77	19.38	18.30	17.63	17.31	17.45
Cr <sub>2</sub> O <sub>3</sub>	0.00	0.02	0.03	0.00	0.21	0.04	0.00	0.00
FeO	38.25	44.26	43.23	40.52	43.10	23.55	22.43	24.37
MnO	1.70	1.04	1.23	1.43	1.07	1.67	1.60	1.80
MgO	3.80	0.27	0.61	2.89	2.14	15.24	16.05	14.82
CaO	0.02	0.17	0.05	0.10	0.00	0.06	0.00	0.00
K <sub>2</sub> O	0.01	0.00	0.00	0.02	0.00	0.02	0.00	0.02
Na <sub>2</sub> O	0.02	0.02	0.04	0.02	0.00	0.01	0.01	0.00
ZnO	0.01	0.00	0.00	0.00	0.00	0.13	0.11	0.12
F	0.81	0.00	0.00	0.00	0.90	0.36	0.43	0.55
Total	87.47	87.23	86.63	87.51	88.09	86.07	85.15	86.54
Cations calculated on the basis of 28 oxygen atoms								
Si	2.76	2.64	2.61	2.74	2.69	3.17	3.19	3.18
Ti	0.00	0.00	0.00	0.00	0.00	0.00	0.00	0.00
AlIV	1.24	1.36	1.39	1.26	1.31	0.83	0.81	0.82
AlVI	1.50	1.39	1.42	1.44	1.29	1.58	1.58	1.56
Cr	0.00	0.00	0.00	0.00	0.02	0.00	0.00	0.00
Fe <sup>2+</sup>	3.80	4.44	4.36	4.01	4.34	2.29	2.20	2.36
Mn	0.17	0.11	0.13	0.14	0.11	0.16	0.16	0.18
Mg	0.40	0.03	0.06	0.30	0.23	1.56	1.66	1.52
Ca	0.00	0.02	0.01	0.01	0.00	0.01	0.00	0.00
K	0.00	0.00	0.00	0.00	0.00	0.00	0.00	0.00
Na	0.00	0.00	0.01	0.00	0.00	0.00	0.00	0.00
Zn	0.00	0.00	0.00	0.00	0.00	0.01	0.01	0.01
F	0.30	0.00	0.00	0.00	0.34	0.13	0.16	0.20
Fe/Fe + Mg	0.90	0.99	0.99	0.93	0.95	0.59	0.57	0.61
Mg/Mg + Fe	0.10	0.01	0.01	0.07	0.05	0.41	0.43	0.39
Al/(Al + Fe + Mg)	0.39	0.38	0.39	0.39	0.36	0.39	0.38	0.38
T	280.3	305.9	313.2	285.9	295.6	193.6	189.9	192.9

## 7. Discussion

### 7.1. Element Migration and Implication for the Genesis of the Nuocang Skarn

Generally, systematic examination of skarn geochemical features from different zones within the skarn deposit could help to understand the element migration process, spatial distribution, and the genesis of skarn deposits [3,4]. The Nuocang deposit is characterized by well developed skarn and relatively obvious skarn zoning. The exoskarn rocks near the limestone are commonly formed as veinlets in the limestone, indicating that the original protolith for the pyroxene-rich skarn was limestone. The endoskarn rocks are spatially associated with ore-related granite porphyry, with a distinct garnet-epidote alteration in the endoskarn (Figure 3c). These zonal arrangements of skarns from the limestone, through the skarn zone, and hornfels, to the igneous rock, indicate an infiltration-driven metasomatic origin, and the compositional variations in the skarns are generally thought to be induced by the metasomatic transfer of various components from the volatile crystallizing saturated granite porphyry [42].

The scatter diagrams of mass-balance calculations could also provide some information for the metasomatic formation of the skarn. Compared with the unaltered protolithic limestone in the Nuocang deposit (Figure 10), the chemical composition of garnet-pyroxene skarn and pyroxene-rich skarns are

enriched in  $\text{SiO}_2$ ,  $\text{Fe}_2\text{O}_3^{\text{T}}$ , and  $\text{MnO}$ , and much less  $\text{CaO}$ ,  $\text{MgO}$ ,  $\text{K}_2\text{O}$ , and  $\text{P}_2\text{O}_5$ . However, compared with the unaltered sandstone, the skarnified hornfels and sandstone, and muscovite-garnet-pyroxene skarn are enriched in  $\text{Fe}_2\text{O}_3^{\text{T}}$ ,  $\text{CaO}$ , and  $\text{MnO}$ , and depleted in  $\text{SiO}_2$ ,  $\text{MgO}$ ,  $\text{Na}_2\text{O}$ ,  $\text{K}_2\text{O}$ , and  $\text{P}_2\text{O}_5$ . This result indicates that the Ca in the skarn minerals was provided by the limestone, whereas the magmatic fluids were the main source for Si (except that in skarnified hornfels and sandstone, and muscovite-garnet-pyroxene skarn), Fe, Mn and base-metals. In the skarnified hornfels and sandstone, and muscovite-garnet-pyroxene skarn (Figure 10), the protolithic sandstone could supply the Si, Mg, K, and P, whereas the limestone could supply Ca, and the magmatic fluid supplied Fe and Mn.

Generally, the sandstone from a strong reduced depositional environment is enriched in Ca, Al, and Ti [43], which explain that the garnet in the endoskarn is enriched in the grossular composition. Additionally, the magmatic fluids migrated along the fractures and metasomatized the limestone, leading to the formation of skarn minerals such as the Mn-rich hedenbergite. Therefore, the Fe, Mn and base-metals concentrated in the exoskarn, is mainly due to migration exsolved metalliferous brines from the granite porphyry infiltrating into the host rocks [44].

The calculated mass changes for trace elements are shown in the Table 3. Most of the LILE elements (Figure 10), such as the Rb, Ba, and Li display visible mass loss in the altered rocks, especially in the skarnified hornfels and sandstone, and muscovite-garnet-pyroxene skarn. The depletion of these elements means that they were brought out from the preexisting rocks by magmatic fluids. Regarding Sr, this element shows a generalized mass loss in the garnet-pyroxene skarn and pyroxene-rich skarn but increased its content in the skarnified hornfels and sandstone. and in the muscovite-garnet-hedenbergite skarn. Generally, the Sr is enriched in grossularite skarn and garnet-epidote skarn, which possibly was caused by the residual plagioclase or other Ca-rich minerals. The HFSE elements of Zr, Hf, Nb, Ta, U, and Th behaved as immobile elements in the skarn stage [22–24,45–47]. In this study, the Nb, Ta, and U seem unchanged in the skarn (Figure 10). However, the Zr, Hf, and Th display very minimal changes in the garnet-pyroxene skarn and pyroxene-rich skarn but generated notable mass gain in the skarnified hornfels and sandstone, and muscovite-garnet-pyroxene skarn (Figure 10). The ore-forming elements Pb and Zn in the garnet-pyroxene skarn and pyroxene-rich skarn generated mass gain, indicating that the Pb-Zn deposits usually develop in the distal skarn (Figure 7). However, Sn received mass gain in both the endoskarn and exoskarn, suggesting that Sn was supplied by the ore-forming intrusion as well. This feature is supported by the high contents of Sn present in the ore-forming intrusive bodies. The copper in the garnet-pyroxene skarn and pyroxene-rich skarn shows very minor changes, but generated mass loss in the skarnified sandstone and the muscovite-garnet-pyroxene skarn, considering that chalcopyrite only occurs in the skarnified sandstone, muscovite-garnet-pyroxene skarn, and the fracture surfaces of the sandstone.

The REEs in most skarns also show similar patterns with the igneous rocks. The skarnified hornfels and sandstone, and muscovite-garnet-pyroxene skarn exhibit relatively higher contents of REEs than that in the exoskarn (strong alteration and mineralization). Moreover, the  $\sum\text{REEs}$  contents in zone 9 (strongly silicified and mineralized pyroxene-rich skarn zone), have the lowest total REE contents, suggesting that the strong alteration and mineralization will decrease the REEs contents extensively. These features indicate the REEs were sourced from magmatic-hydrothermal fluids of the igneous rock, which migrated with complexing agents such as Cl, F,  $\text{HCO}_3^-$ , exchanged elements with the limestone, and were enriched in the skarn [48,49]. Thus, skarn geochemistry and mineral assemblages indicate the skarn in the Nuocang deposit is typical of magmatic hydrothermal metasomatic genetic type.

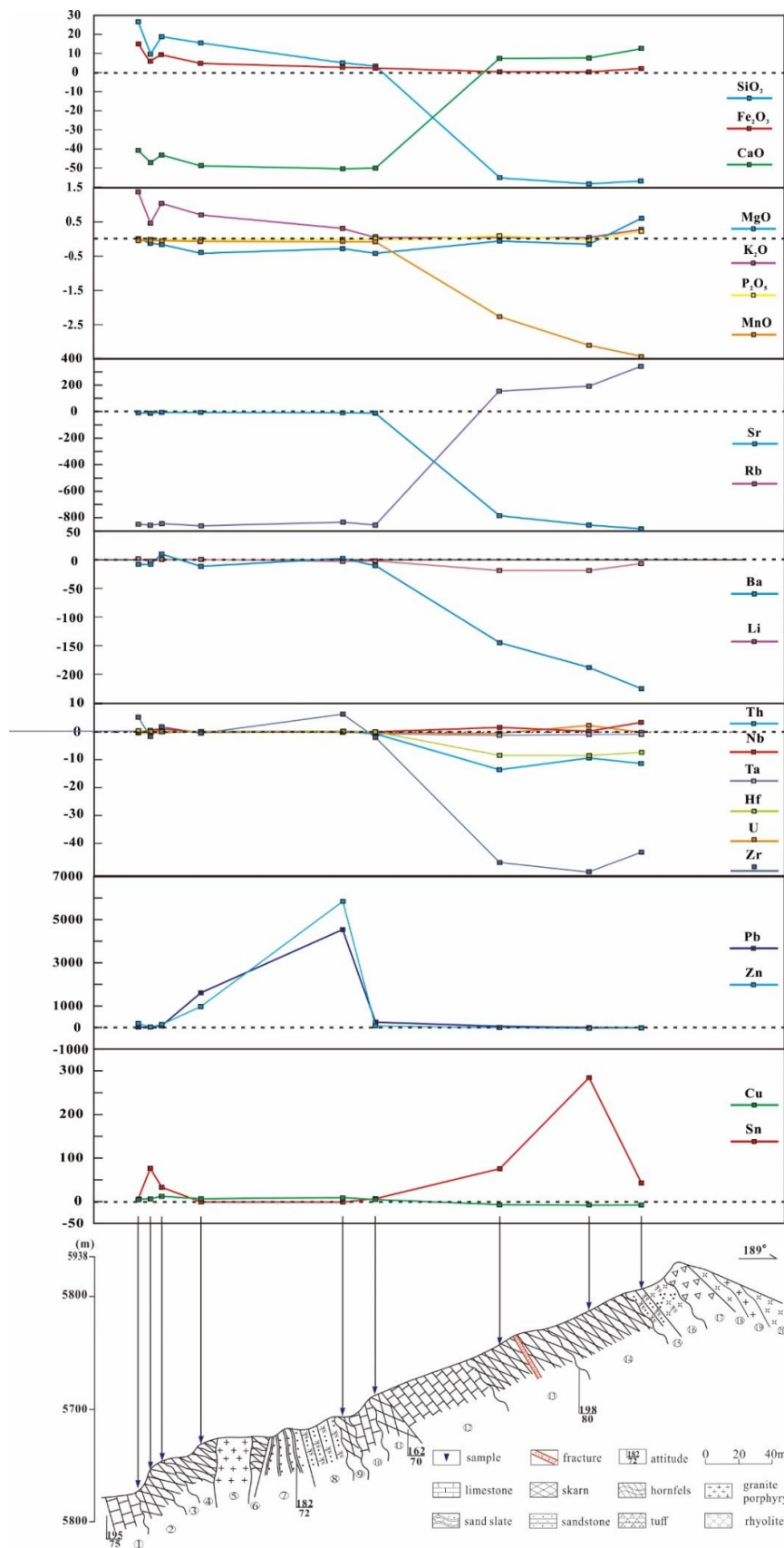
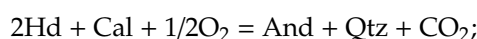


**Figure 10.** Mass change scatter diagrams of major and trace elements in the skarn section of Nuocang deposit.

## 7.2. Skarn Formation Conditions and Hydrothermal Evolution

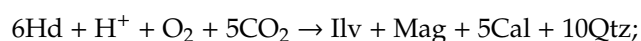
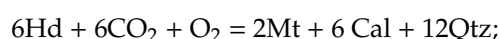
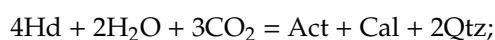
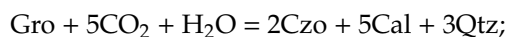
Compositional variations in the skarn minerals could provide some valid information for magma chemistry, wall rock component, and oxidation state [6,50]. The earliest change in meta-sedimentary rocks of the Angren Formation involves the formation of hornfels. Based on the distinctive porphyritic texture of granite porphyry, the Pb-Zn mineralization occurring in the brittle fracture zone, the weak thermal metamorphism, the lateral extended skarnification outwards (structural controls) rather than following the intrusive contacts, and also the scarce high salinity in garnet fluid inclusions (unpublished data from Junsheng Jiang) in the Nuocang deposit; all these evidences would suggest that the skarn formed in a hypabyssal environment. The minor wollastonite associated with pyroxene indicates  $X_{(\text{CO}_2)} < 0.1$  during the prograde stage [51].

In the prograde stage, garnet I (andradite-dominant) was the earliest product of skarn crystallization. It is euhedral and relatively homogeneous, due to the sufficient mineral-forming ingredient supply and growth space [52,53]. Generally, andradite-bearing assemblages are indicative that the initial ore fluids were of high temperature and oxidized. The subsequent substitution of Fe by Al in andradite indicates the gradually decreasing fluid oxygen fugacity, which results in a distinct oscillatory zoning in garnet II and III. With further magmatic fractionation, decreasing temperature, and oxygen fugacity, significant exsolution of metalliferous magmatic fluids infiltrated and migrated along the reactivated faults or other fractures for a long distance, before reacting with the contact of the Angjie Formation limestone. Under these circumstances, pyroxene was generated in a disequilibrium geochemical system through the infiltrative metasomatism between magmatic fluids and limestone. The poikilitic textures of garnet suggest that part of garnet formed later than pyroxene (“overgrown-pseudomorph”, Figure 4f). In addition, EPMA data show an increase of andradite from core to rim in garnet IV whereas the hedenbergite in pyroxene II decreases dramatically outwards (Tables 2 and 3; Figure 7b,d). This compositional variation of garnet and pyroxene could be possibly caused by the following reaction [54]:



Through this redox reaction, it would have decreased the oxygen fugacity of ore-forming fluid. Meanwhile, the aluminum content of garnet decreased from core to rim, indicating that the fluids vary from low W/R (water/rock) ratios of local pore fluids to dominant magmatic hydrothermal fluids.

With the decreasing temperature and increasing oxygen fugacity and hydrolysis, early retrograde alteration occurred. The early retrograde stage (stage II) was characterized by hydrous skarn minerals assemblages, such as epidote/clinozoisite, actinolite, ilvaite, as replacement phases after garnet and pyroxene. The occurrence of these hydrous calc-silicates can be explained by the following reactions [55,56]:



Generally, ilvaite compositions in Fe skarn deposits are more Fe-rich than those of Zn–Pb deposits, which are Mn-rich. The varying Fe–Mn content of ilvaite from Fe to Pb–Zn skarns may be as a consequence of a decrease in temperature [27]. Meanwhile, the occurrence of hydrous skarn minerals needs large amounts of oxygen, which means that in the early retrograde stage have a higher oxygen fugacity than that of prograde stage. Obviously, the ilvaite from the Nuocang deposit shows low Fe and high Mn contents, is consistent with that of high Mn contents in the pyroxene.

The continuous metasomatic reactions between the hydrothermal fluids and limestone in Nuocang deposit suggest a gradual decreasing temperature. With the mixing of meteoric water, the oxygen

fugacity gradually increased, resulting in the formation of chlorite, muscovite, together with small amounts of pyrite-chalcopyrite-pyrrhotite-quartz in the late retrograde skarn stage. The Fe-rich chlorite (chamosite) formed in a relatively more reduced and acid environment than that of the Mg-rich chlorite [57]. Chlorite I with pyrite-chalcopyrite-pyrrhotite-quartz is relatively enriched in Fe, revealing that they formed in the acid and relatively reduced environment during the late retrograde stage. This result is in agreement with the relatively low  $Fe^{3+}/Fe^{2+}$  values (0.32–0.73) of the muscovite. Chlorite I yields calculated formation temperatures from 336 to 386 °C (mean of 361 °C, [58]), which are in line with the homogeneous temperatures of fluid inclusion in the late retrograde stage (unpublished data from Junsheng Jiang). Chlorite I forms as a result of dissolution–migration–precipitation [59], namely that the hydrothermal fluids leached out Fe and Mg from the ferromagnesian minerals and transported them along the fracture, joints or mineral fissures to other locations, precipitated in the form of chlorite and associated minor Fe–Cu mineralization. Subsequently, the Pb–Zn ore-forming fluids continued to migrate to farther distance due to its high mobility. Migration of the ore-forming hydrothermal fluids through open spaces, and their mixing with increasing amounts of meteoric waters, resulted to a temperature decrease and reduction of the solubility of metal-chlorine complexes [60,61]. Thus, the change of ore-forming fluid physicochemical conditions would lead to significant Pb–Zn sulfide saturation. After the sulfides deposition, the continued mixing with large amounts of cold meteoric water would decrease its temperature, and increase its pH value (neutralizing), promoting the deposition of significant amounts of calcite and chlorite II (199–205 °C, average temperature: 203 °C). After exhumation, weathering processes oxidized sulfides mainly producing supergene phases such as malachite, azurite, and cerussite.

### 7.3. Implication for the Deposit Type and Mineralization Potential

The geological, mineralogical, and geochemical characteristics of Nuocang skarn are indicative of a typical calcic skarn. The Nuocang skarn mainly consists of calc-silicate mineral assemblages, such as the hedenbergite-dominant pyroxene (up to 80%), grossular–andradite garnet, epidote, ilvaite, chlorite, and muscovite. The mineralization mainly occurs in the exoskarn, and the contents of hedenbergite and johannsenite are relatively high, which are considered as a distinctive feature of Zn-rich skarns [26,51,54,61], Figure 8a). As summarized by Nakano et al. [62], most pyroxenes of Cu–Fe deposits have a low Mn/Fe ratio (<0.1), whereas the pyroxene of Pb–Zn deposits are featured by a high Mn/Fe ratio (>0.2). The Mn/Fe ratios in the Nuocang pyroxene generally range from 0.07 to 0.34 (mean 0.14), suggesting that the Nuocang is genetically a polymetallic deposit. Although ilvaite is a relatively rare mineral, its complex formula and its compositional variability could provide some information for identifying the skarn deposit type and discussing the ore-forming geological environment [26,31,51]. The ilvaite from Fe–Cu–Au and W–Mo skarns contains more Fe and less Mn than ilvaite from the Pb–Zn skarn. The ilvaite from Sn skarn has the lowest Mn and  $Fe^{3+}$  of all skarn types, with total Fe contents intermediate between that of Zn and Fe–Cu–Au skarn. The ilvaite I in the Nuocang deposit plotted close to W–Mo deposits, whereas the ilvaite II plotted close to the Pb–Zn deposits, indicating that the Nuocang deposit is of a Pb–Zn polymetallic type (Figure 9). Additionally, the selected samples from Nuocang deposit yield an average grade of 0.065%  $WO_3$  [18], reaching the accompanying grade of tungsten ore), also indicating the characteristics of a Pb–Zn polymetallic deposit (Figure 9).

The Linzizong volcanic rocks, as a major component of Andean-type continental margin along South Asia, extend in an elongate area of ~1000 × 200 km [63,64]. In contrast with the widespread porphyry-epithermal Cu–Au–Ag deposits in the volcanic area of the Andes metallogenic belt, relatively few porphyry-epithermal deposits have been discovered in the Linzizong volcanic area. The discovered deposits hosted in the Linzizong volcanic area comprises the Narusongduo epithermal (cryptoexplosive breccia type-hydrothermal vein)-skarn type Pb–Zn–Ag, the Sinongduo epithermal-skarn type Pb–Zn–Ag, and the Nuocang skarn type Pb–Zn polymetallic, the Zhazhalong and the Dexin epithermal (hydrothermal vein type) Pb–Zn deposits [29,65,66]. In comparison, the Nuocang

Pb-Zn polymetallic skarn deposit displays some general geological, geochemical, and mineralogical similarities to those of Narusongduo and Sinongduo. Generally, the ore-related granite porphyry occurs as stocks or dykes in the Linzizong volcanic rocks, and show temporal affinity with the Linzizong volcanic rocks, e.g., Nuocang granite porphyry of  $72.4 \pm 0.6$  Ma and  $73.4 \pm 0.7$  Ma, and rhyolite of  $72.4 \pm 0.4$  Ma [19]; Narusongduo granite porphyry of  $62.5 \pm 0.8$  Ma, and rhyolite crystal tuff of 61.7 Ma [67]; Sinongduo granite porphyry of  $68.2 \pm 0.3$  Ma, and rhyolite of 62–65 Ma [68,69], which are the subvolcanic rocks of Linzizong volcanic rocks. All these features reveal that these deposits are spatially and temporally associated with late Cretaceous to Paleocene Linzizong volcanic activity [70–72]. During this period, the rollback of the northward subducting Neo-Tethyan ocean lithosphere induced the formation of extensive I-type calc-alkaline to high-K Linzizong volcanic rocks, and coeval plutons, which have supplied the initial ore-forming fluids for these deposits. So far, except the skarn-type orebodies that have been discovered in the Narusongduo and Sinongduo deposits, a series of epithermal type (crypto-explosion breccia and vein type) orebodies have been discovered in the Linzizong volcanic rocks. These orebodies generally developed in the volcanic conduit and the off-lying cracks or around the sub-volcanic porphyry intrusion, which formed the most economical orebodies in the deposits, and belong to the typical epithermal deposits.

The skarn-type ore mainly occurs in the eastern part of Nuocang ore district, and hydrothermal quartz vein-type ore only occurred in the western part of Nuocang ore district. The compositions of Nuocang garnet also display a transition from andradite-grossular solid solution in the east to andradite-dominant in the west. Similarly, the exploration geochemistry data (unpublished) also shows that the center of W-Mo-Cu-Pb-Zn-Ag anomaly is also to the southeast of the orebodies. All information discussed above indicates that the ore-forming hydrothermal center is to the southeast, corresponding to the Linzizong volcanic rocks and coeval subvolcanic granite porphyries located to the southeast of the skarn orebodies. In addition, to the southeast of the skarn orebodies, the volcanic breccia is located along the mountain ridge, and to the outer turning into large area of rhyolite, and minor of basaltic andesitic tuff, and andesitic tuff, with the subvolcanic rocks (granite porphyry) occurring as radial veins, which indicate that a volcanic conduit possibly existed there. Combined with the geological characteristics of Sinongduo epithermal orebodies [29], it indicates that the Nuocang region has the exploration potential for both skarn and epithermal mineralization.

## 8. Conclusions

The Nuocang calcic skarn Pb-Zn deposit is featured by a well zoned occurrence. The litho-geochemistry, mineral composition and textural characteristics indicate that the polymetallic zoned skarn was formed by the infiltrative metasomatism of magmatic hydrothermal fluids. The Nuocang deposit comprises four stages, including the prograde skarn, retrograde skarn, sulfide, and supergene stages. The garnet in the prograde stage indicates a moderate oxygen and high temperature environment. In the retrograde stage, the temperature decreased and oxygen fugacity increased, but hydrolysis increased with epidote, ilvaite, chlorite I, and muscovite forming with magnetite. The continuing decreasing temperature and mixing with meteoric water lead to Cu, Pb, and Zn saturation as sulfides. After the sulfides deposition, the continued mixing with large amounts of cold meteoric water would decrease its temperature, and increase its pH value (neutralizing), promoting the deposition of significant amounts of calcite and chlorite II. The geological, mineralogical, and geochemical characteristics of Nuocang skarn, suggest that the Nuocang deposit is of a Pb-Zn polymetallic type. Compared to the other typical skarn-epithermal deposits in the Linzizong volcanic area, it indicates that the Nuocang deposit may have the exploration potential for both skarn and epithermal styles of mineralization.

**Author Contributions:** J.J. and S.G. conceived this contribution and conducted all field and analytical work, assisted by Y.Z., D.R.L., W.X., J.H., J.L., K.T., and X.J. The manuscript was written by J.J. and S.G., with contribution from Y.Z., D.R.L., W.X., J.H., J.L., K.T., and X.J. All authors have read and agreed to the published version of the manuscript.

**Funding:** J.J. acknowledges support from the China Geological Survey (DD20201153, DD20190443, DD20190159-33, DD20160027-2), Commonwealth Project from the National Key Research and Development Program of China (No. 2016YFC0600300), Ministry of Land and Resources (201511015), Changjiang Scholars and Innovative Research Team in University (IRT14R56, IRT1083). D.R.L. is supported by a NSERC Discovery grant.

**Acknowledgments:** Staffs at Wuhan Sample Solution Analytical Technology Co., Ltd. and the Center for Material Research and Analysis, Wuhan University of Technology are gratefully acknowledged for assistance with instrument operation. We thank the reviewers for the journal Minerals.

**Conflicts of Interest:** The authors declare no conflict of interest.

## References

1. Meinert, L.D. Compositional variation of igneous rocks associated with skarn deposits—Chemical evidence for a genetic connection between petrogenesis and mineralization. Mineralogical Association of Canada. *Short Course Ser.* **1955**, *23*, 401–418.
2. Meinert, L.D.; Dipple, G.M.; Nicolescu, S. *World Skarn Deposits; Economic Geology 100th Anniversary*: Littleton, CO, USA, 2005; Volume 299–336.
3. Xu, J.; Ciobanu, C.L.; Cook, N.J.; Zheng, Y.Y.; Sun, X.; Wade, P.B. Skarn formation and trace elements in garnet and associated minerals from Zhibula copper deposit, Gangdese belt, southern Tibet. *Lithos* **2016**, *262*, 213–231. [[CrossRef](#)]
4. Ma, W.; Liu, Y.C.; Yang, Z.S.; Hou, Z.Q.; Li, Z.Q.; Zhao, X.Y.; Fei, F. Alteration, mineralization, and genesis of the Lietinggang–Leqingla Pb–Zn–Fe–Cu–Mo skarn deposit, Tibet, China. *Ore Geol. Rev.* **2017**, *90*, 897–912. [[CrossRef](#)]
5. Wang, X.D.; Wei, W.; Lv, X.B.; Fan, X.J.; Wang, S.B. Stanniferous magnetite composition from the Haobugao skarn Fe–Zn deposit, southern Great Xing’an Range: Implication for mineral depositional mechanism. *Geol. J.* **2017**, *53*, 1823–1839. [[CrossRef](#)]
6. Meinert, L.D. Application of skarn deposit zonation models to mineral exploration. *Explor. Mineral. Geol.* **1997**, *6*, 185–208.
7. Gaspar, M.; Knaack, C.; Meinert, L.D.; Moretti, R. REE in skarn systems: A LA–ICP–MS study of garnets from the Crown Jewel gold deposit. *Geochim. Cosmochim. Acta* **2008**, *72*, 185–205. [[CrossRef](#)]
8. Yin, A.; Harrison, T.M. Geologic evolution of the Himalayan–Tibetan orogen. *Annu. Rev. Earth Planet. Sci.* **2000**, *28*, 211–280. [[CrossRef](#)]
9. Zhu, D.C.; Zhao, Z.D.; Niu, Y.L.; Mo, X.X.; Chung, S.L.; Hou, Z.Q.; Wang, L.Q.; Wu, F.Y. The Lhasa terrane: Record of a microcontinent and its histories of drift and growth. *Earth Planet. Sci. Lett.* **2011**, *301*, 241–255. [[CrossRef](#)]
10. Hou, Z.Q.; Duan, L.F.; Lu, Y.J.; Zheng, Y.C.; Zhu, D.C.; Yang, Z.M.; Yang, Z.S.; Wang, B.D.; Pei, Y.R.; Zhao, Z.D.; et al. Lithospheric architecture of the Lhasa Terrane and its control on ore deposits in the Himalayan–Tibetan Orogen. *Econ. Geol.* **2015**, *110*, 1541–1575. [[CrossRef](#)]
11. Allégre, C.J.; Courtillot, V.; Taponnier, P.; Hirn, A.; Mattauer, M.; Coulon, C.; Jaeger, J.J.; Achache, J.; Schärer, U.; Marcoux, J.; et al. Structure and evolution of the Himalayan–Tibet orogenic belt. *Nature* **1984**, *307*, 17–22. [[CrossRef](#)]
12. Chung, S.L.; Chu, M.F.; Zhang, Y.Q.; Xie, Y.W.; Lo, C.H.; Lee, T.Y.; Lan, C.Y.; Li, X.H.; Zhang, Q.; Wang, Y.Z. Tibetan tectonic evolution inferred from spatial and temporal variations in post-collisional magmatism. *Earth Sci. Rev.* **2005**, *68*, 173–196. [[CrossRef](#)]
13. Zhu, D.C.; Pan, G.T.; Chung, S.L.; Liao, Z.L.; Wang, L.Q.; Li, G.M. SHRIMP zircon age and geochemical constraints on the origin of lower Jurassic volcanic rocks from the Yeba Formation, southern Gangdese, South Tibet. *Int. Geol. Rev.* **2008**, *50*, 442–471. [[CrossRef](#)]
14. Ji, W.Q.; Wu, F.Y.; Chung, S.L.; Li, J.X.; Liu, C.Z. Zircon U–Pb geochronology and Hf isotopic constraints on petrogenesis of the Gangdese batholith, southern Tibet. *Chem. Geol.* **2009**, *262*, 229–245. [[CrossRef](#)]
15. Zheng, Y.Y.; Sun, X.; Gao, S.B.; Wang, C.M.; Zhao, Z.Y.; Wu, S.; Li, J.D.; Wu, X. Analysis of stream sediment data for exploring the Zhunuo porphyry Cu deposit, southern Tibet. *J. Geochem. Explor.* **2014**, *143*, 19–30. [[CrossRef](#)]
16. Zheng, Y.Y.; Sun, X.; Gao, S.B.; Zhao, Z.D.; Zhang, G.Y.; Wu, S.; You, Z.M.; Li, J.D. Multiple mineralization events at the Jiru porphyry copper deposit, southern Tibet: Implications for Eocene and Miocene magma sources and resource potential. *J. Asian Earth Sci.* **2014**, *79*, 842–857. [[CrossRef](#)]

17. Gao, S.B.; Zheng, Y.Y.; Tian, L.M.; Zhang, Z.; Qu, W.J.; Liu, M.Y.; Zheng, H.T.; Zheng, L.; Zhu, J.H. Geochronology of magmatic intrusions and mineralization of Chagele copper-lead-zinc deposit in Tibet and its implications. *Earth Sci. J. China Univ. Geosci.* **2012**, *37*, 507–513.
18. Yao, S.; Li, P.; Guo, X.F.; Lu, X.J.; Zhang, X.T. Ore-forming geological characteristics and prospecting perspective analysis of the Magui lead-zinc polymetallic ore deposit in Tibet. *Geol. Bull. China* **2016**, *35*, 1529–15359.
19. Jiang, J.S.; Zheng, Y.Y.; Gao, S.B.; Zhang, Y.C.; Huang, J.; Liu, J.; Wu, S.; Xu, J.; Huang, L.L. The newly-discovered Late Cretaceous igneous rocks in the Nuocang district: Products of ancient crust melting triggered by Neo-Tethyan slab rollback in the western Gangdese. *Lithos* **2018**, *308–309*, 294–315. [[CrossRef](#)]
20. Liu, Y.S.; Hu, Z.C.; Gao, S.; Günther, D.; Xu, J.; Gao, C.G.; Chen, H.H. In situ analysis of major and trace elements of anhydrous minerals by LA-ICP-MS without applying an internal standard. *Chem. Geol.* **2008**, *257*, 34–43. [[CrossRef](#)]
21. Guo, S.; Ye, K.; Chen, Y.; Liu, J.B. A normalization solution to mass transfer illustration of multiple progressively altered samples using the isocon diagram. *Econ. Geol.* **2009**, *104*, 881–886. [[CrossRef](#)]
22. Gresens, R.L. Composition-volume relationships of metasomatism. *Chem. Geol.* **1967**, *2*, 47–65. [[CrossRef](#)]
23. Grant, J.A. The isocon diagram; a simple solution to Gresens' equation for metasomatic alteration. *Econ. Geol.* **1986**, *81*, 1976–1982. [[CrossRef](#)]
24. MacLean, W.H.; Barrett, T.J. Lithochemical techniques using immobile elements. *J. Geochem. Explor.* **1993**, *48*, 109–133. [[CrossRef](#)]
25. Franchini, M.B.; Meinert, L.D.; Valles, J.M. First occurrence of ilvaite in a gold skarn deposit. *Econ. Geol.* **2002**, *97*, 1119–1126. [[CrossRef](#)]
26. Bonev, I.K.; Vassileva, R.D.; Zotov, N.; Kouzmanov, K. Manganilvaite,  $\text{CaFe}^{2+}\text{Fe}^{3+}(\text{Mn,Fe}^{2+})(\text{Si}_2\text{O}_7)\text{O}(\text{OH})$ , a new mineral of the ilvaite group from Pb-Zn skarn deposits in the Rhodope Mountains. *Bulg. Can. Mineral.* **2005**, *43*, 1027–1042. [[CrossRef](#)]
27. Yu, M. *Metallogenic Mechanism of the Galinge Polymetallic Iron Skarn Deposit, Qiman Tagh Mountains, Qinghai Province*; Springer Theses: Berlin/Heidelberg, Germany, 2019. [[CrossRef](#)]
28. Huang, H.; Zhang, C.Q.; Zhou, Y.M.; Liu, B.; Xie, Y.F.; Dong, Y.T.; Yang, C.H.; Dong, W.W. Skarn mineralogy and zoning model of the Jinchanghe copper-zinc-iron polymetallic deposit in Yunnan Province. *Acta Petrol. Min.* **2014**, *33*, 127–148.
29. Li, X.F.; Wang, C.Z.; Mao, W.; Xu, Q.H.; Liu, Y.H. The fault-controlled skarn W–Mo polymetallic mineralization during the main India–Eurasia collision: Example from Hahaigang deposit of Gangdese metallogenic belt of Tibet. *Ore Geol. Rev.* **2014**, *58*, 27–40. [[CrossRef](#)]
30. Gole, M.J. Ca–Fe–Si skarn containing babingtonite: First known occurrence in Australia. *Can. Mineral.* **1981**, *19*, 26–277.
31. Meinert, L.D. Mineralogy and petrology of iron skarns in western British Columbia, Canada. *Econ. Geol.* **1984**, *79*, 869–882. [[CrossRef](#)]
32. Tang, P.Z. The Geochemistry Characteristics of Cihai Iron Deposit in Xinjiang. Master's Thesis, Kunming University of Science and Technology, Kunming, China, 2010.
33. Tang, P.Z.; Wang, Y.W.; Wang, J.B.; Long, L.L.; Zhang, H.Q.; Liao, Z. Finding and significance of ilvaite in the Cihai Iron Deposit, Xinjiang Autonomic Region, China. *Acta Mineral. Sin.* **2011**, *31*, 9–16.
34. Ashley, P.M. Geology of the Ban Ban zinc deposit, a sulfide-bearing skarn, Southeast Queensland, Australia. *Econ. Geol.* **1980**, *75*, 15–29. [[CrossRef](#)]
35. Meinert, L.D. Skarn zonation and fluid evolution in the Groundhog mine, Central Mining district, New Mexico. *Econ. Geol.* **1987**, *82*, 523–545. [[CrossRef](#)]
36. Kwak, T.P. The geology and geochemistry of the zoned, Sn–W–F–Be skarns at Mt. Lindsay, Tasmania, Australia. *Econ. Geol.* **1983**, *78*, 1440–1465. [[CrossRef](#)]
37. Graser, G.; Markl, G. Ca-rich ilvaite–epidote–hydrogarnet endoskarns: A record of late magmatic fluid influx into the perisodic Ilímaussaq complex, South Greenland. *J. Petrol.* **2008**, *49*, 239–265. [[CrossRef](#)]
38. Deer, W.A.; Howie, R.A.; Zussman, J. *An Introduction to the Rock-Forming Minerals*; Longman Group Ltd.: New York, NY, USA, 1992; pp. 1–696.
39. Foster, M.D. *Interpretation of the Composition and Classification of the Chlorites*; US Geology Survey: Reston, VA, USA, 1962; pp. 1–33.

40. Zang, W.; Fyfe, W.S. Chloritization of the hydrothermally altered bedrock at the Igarape Bahia gold deposit, Carajas, Brazil. *Mineral. Depos.* **1995**, *30*, 30–38. [[CrossRef](#)]
41. Laird, J. Chlorites: Metamorphic petrology. *Rev. Mineral. Geochem.* **1988**, *19*, 405–453.
42. Lentz, D.R.; Suzuki, K. A low F pegmatite-related Mo skarn from the southwestern Grenville Province, Ontario, Canada: Phase equilibria and petrogenetic implications. *Econ. Geol.* **2000**, *95*, 1319–1337. [[CrossRef](#)]
43. Einaudi, M.T.; Meinert, L.D.; Newberry, R.J. Skarn deposits. In *Economic Geology Seventy-Fifth Anniversary Volume*; Skinner, B.J., Ed.; Society of Economic Geologists: Boulder, Colorado, 1981; pp. 317–391.
44. Harris, N.B.; Einaudi, M.T. Skarn deposits in the Yerington district, Nevada; metasomatic skarn evolution near Ludwig. *Econ. Geol.* **1982**, *77*, 877–898. [[CrossRef](#)]
45. Leitch, C.H.B.; Lentz, D.R. The Gresen's approach to mass balance constraints of alteration systems: Methods, pitfalls, examples. In *Alteration and Alteration Processes Associated with Ore-Forming Systems*; Geological Association of Canada, Short Course Notes; Lentz, D.R., Ed.; Geological Association of Canada: Ottawa, ON, Canada, 1994; Volume 11, pp. 161–192.
46. Ague, J.J. Extreme channelization of fluid and the problem of element mobility during Barrovian metamorphism. *Am. Mineral.* **2011**, *96*, 333–352. [[CrossRef](#)]
47. Brauhart, C.W.; Huston, D.L.; Groves, D.I.; Mikucki, E.J.; Gardoll, A.S. Geochemical mass-transfer patterns as indicators of the architecture of a complete volcanic-hosted massive sulfide hydrothermal alteration system, Panorama district, Pilbara, Western Australia. *Econ. Geol.* **2001**, *96*, 1263–1278. [[CrossRef](#)]
48. Flynn, R.T.; Burnham, C.W. An experimental determination of rare earth partition coefficients between a chloride containing vapour phase and silicate melts. *Geochim. Cosmochim. Acta* **1978**, *42*, 685–701. [[CrossRef](#)]
49. Humphris, S.E. The mobility of rare earth elements in the crust. In *Rare Earth Element Geochemistry*; Henderson, P., Ed.; Elsevier: New York, NY, USA, 1984; pp. 317–342.
50. Burton, J.C.; Taylor, L.A.; Chou, I.-M. The  $f_{O_2}$ -T and  $f_{S_2}$ -T stability relations of hedenbergite and of hedenbergite–johannsenite solid solutions. *Econ. Geol.* **1982**, *77*, 764–783. [[CrossRef](#)]
51. Canet, C.; Camprubí, A.; González-Partida, E.; Linares, C.; Alfonso, P.; Piñero-Fernández, F.; Prol-Ledesma, R.M. Mineral assemblages of the Francisco I. Madero Zn–Cu–Pb–(Ag) deposit, Zacatecas, Mexico: Implications for ore deposit genesis. *Ore Geol. Rev.* **2009**, *35*, 423–435. [[CrossRef](#)]
52. Meinert, L.D.; Hedenquist, J.W.; Satoh, H.; Matsuhisa, Y. Formation of anhydrous and hydrous skarn in Cu–Au ore deposits by magmatic fluids. *Econ. Geol.* **2003**, *98*, 147–156. [[CrossRef](#)]
53. Peng, H.J.; Zhang, C.Q.; Mao, J.W.; Santosh, M.; Zhou, Y.M.; Hou, L. Garnets in porphyry–skarn systems: A LA–ICP–MS, fluid inclusion, and stable isotope study of garnets from the Hongniu–Hongshan copper deposit, Zhongdian area, NW Yunnan Province, China. *J. Asian Earth Sci.* **2015**, *103*, 229–251. [[CrossRef](#)]
54. Logan, M.A.V. Mineralogy and geochemistry of the Gualilán skarn deposit in the Precordillera of western Argentina. *Ore Geol. Rev.* **2000**, *17*, 113–138. [[CrossRef](#)]
55. Berman, R.G.; Brown, T.H.; Greenwood, H.J. Heat capacity of minerals in the system  $Na_2O$ – $K_2O$ – $CaO$ – $MgO$ – $FeO$ – $Fe_2O_3$ – $Al_2O_3$ – $SiO_2$ – $TiO_2$ – $H_2O$ – $O_2$ . *Contrib. Mineral. Petr.* **1985**, *89*, 168–183. [[CrossRef](#)]
56. Deer, W.A.; Howie, R.A.; Zussman, J. *Rock-Forming Minerals. 2B. Double Chain Silicates*; Geological Society: London, UK, 1997; pp. 1–764.
57. Inoue, A. Formation of clay minerals in hydrothermal environments. In *Origin and Mineralogy of Clays*; Springer: Berlin/Heidelberg, Germany, 1995; pp. 268–330.
58. Cathelineau, M. Cation site occupancy in chlorites and illites as function of temperature. *Clay Miner.* **1988**, *23*, 471–485. [[CrossRef](#)]
59. Liao, Z.; Liu, Y.P.; Li, C.Y.; Ye, L.; Liu, S.R.; Zheng, W.Q. Characteristics of chlorites from Dulong Sn–Zn deposit and their metallogenic implications. *Miner. Dep.* **2010**, *29*, 169–176.
60. Barnes, H.L. *Geochemistry of Hydrothermal Ore Deposits*; John Wiley and Sons: New York, NY, USA, 1997; pp. 303–358.
61. Robb, L. *Introduction to Ore-Forming Processes*; John Wiley and Sons: New York, NY, USA, 2009; pp. 129–214.
62. Nakano, T.; Yoshino, T.; Shimazaki, H.; Shimizu, M. Pyroxene composition as an indicator in the classification of skarn deposits. *Econ. Geol.* **1994**, *89*, 1567–1580. [[CrossRef](#)]
63. Mo, X.X.; Hou, Z.Q.; Niu, Y.L.; Dong, G.C.; Qu, X.M.; Zhao, Z.D.; Yang, Z.M. Mantle contributions to crustal thickening during continental collision, evidence from Cenozoic igneous rocks in Southern Tibet. *Lithos* **2007**, *96*, 225–242. [[CrossRef](#)]

64. Mo, X.X.; Niu, Y.L.; Dong, G.C.; Zhao, Z.D.; Hou, Z.Q.; Zhou, S.; Ke, S. Contribution of syncollisional felsic magmatism to continental crust growth: A case study of the Paleogene Linzizong volcanic succession in Southern Tibet. *Chem. Geol.* **2008**, *250*, 49–67. [[CrossRef](#)]
65. Gao, S.B. Copper-Iron Polymetallic Metallogenic Regularity and Election of Target Areas in the Western of Gangdese Metallogenic Belt, Tibet. Ph.D. Thesis, China University of Geosciences, Wuhan, China, 2015; pp. 54–58.
66. Liu, Y.C.; Ji, X.H.; Hou, Z.Q.; Tian, S.H.; Li, Z.P.; Zhao, X.Y.; Zhou, J.S.; Ma, W.; Yang, Z.S. The establishment of an independent Pb-Zn mineralization system related to magmatism: A case study of the Narusongduo Pb-Zn deposit in Tibet. *Acta Petrol. Mineral.* **2015**, *34*, 539–556.
67. Ji, X.H. Study on Geology, Geochemistry and Genesis of Narusongduo Lead-Zinc Deposit, Tibet. Master's Thesis, China University of Geosciences, Beijing, China, 2013; pp. 18–33.
68. Liu, B.; Dong, S.L.; Li, G.M.; Zhang, H. Geochemistry and chronology characteristics of the intrusion at the Sinongduo Pb-Zn deposit, Tibet. *Miner. Depos.* **2010**, *29*, 472–473. (In Chinese)
69. Ding, S.; Chen, Y.C.; Tang, J.X.; Xie, F.W.; Hu, G.Y.; Yang, Z.Y.; Shi, S.; Li, Y.H.; Yang, H.Y. Relationship between Linzizong volcanic rocks and mineralization: A case study of Sinongduo epithermal Ag-Pb-Zn deposit. *Miner. Depos.* **2017**, *36*, 1074–1092.
70. Lee, H.Y.; Chung, S.L.; Ji, J.Q.; Qian, Q.; Gallet, S.; Lo, C.H.; Lee, T.Y.; Zhang, Q. Geochemical and Sr-Nd isotopic constraints on the genesis of the Cenozoic Linzizong volcanic successions, southern Tibet. *J. Asian Earth Sci.* **2012**, *53*, 96–114. [[CrossRef](#)]
71. Lee, H.Y.; Chung, S.L.; Lo, C.H.; Ji, J.Q.; Lee, T.Y.; Qian, Q.; Zhang, Q. Eocene Neotethyan slab breakoff in southern Tibet inferred from the Linzizong volcanic record. *Tectonophysics* **2009**, *477*, 20–35. [[CrossRef](#)]
72. Yue, X.Y. Geochemical Characteristics and Significance of Dianzhong Volcanic Rocks in the Cuoqin Area Tibet China. Master's Thesis, Chengdu University of Technology, Chengdu, China, 2012; pp. 35–46.



© 2020 by the authors. Licensee MDPI, Basel, Switzerland. This article is an open access article distributed under the terms and conditions of the Creative Commons Attribution (CC BY) license (<http://creativecommons.org/licenses/by/4.0/>).